

Fuzzification of a Crisp Near-Real-Time Operational Automatic Spectral-Rule-Based Decision-Tree Preliminary Classifier of Multisource Multispectral Remotely Sensed Images

Andrea Baraldi

Abstract—Proposed in recent literature, a novel two-stage stratified hierarchical hybrid remote-sensing image understanding system (RS-IUS) architecture comprises the following: 1) a first-stage pixel-based application-independent top-down (physical-model-driven and prior-knowledge-based) preliminary classifier and 2) a second-stage battery of stratified hierarchical context-sensitive application-dependent modules for class-specific feature extraction and classification. The first-stage preliminary classifier is implemented as an operational automatic near-real-time per-pixel multisource multiresolution application-independent spectral-rule-based decision-tree classifier (SRC). To the best of the author’s knowledge, SRC provides the first operational example of an automatic multisensor multiresolution Earth-observation (EO) system of systems envisaged under ongoing international research programs such as the Global Earth Observation System of Systems (GEOSS) and the Global Monitoring for the Environment and Security (GMES). For the sake of simplicity, the original SRC formulation adopts crisp (hard) membership functions unsuitable for dealing with component cover classes of mixed pixels (class mixture). In this paper, the crisp (hierarchical) SRC first stage of a two-stage hybrid RS-IUS is replaced by a fuzzy (horizontal) SRC. In operational terms, a relative comparison of the fuzzy SRC against its crisp counterpart reveals that the former features the following: 1) the same degree of automation which cannot be surpassed, i.e., they are both “fully automatic”; 2) a superior map information/knowledge representation where component cover classes of mixed pixels are modeled; 3) the same robustness to changes in the input multispectral imagery acquired across time, space, and sensors; 4) a superior maintainability/scalability/reusability guaranteed by an internal horizontal (flat) modular structure independent of hierarchy; and 5) a computation time increased by 30% in a single-process single-thread implementation. This computation overload would reduce to zero in a single-process multithread implementation. In line with theory, the conclusion of this work is that the operational qualities of the fuzzy and crisp SRCs differ, but both SRCs are suitable for the development of operational automatic near-real-time multisensor satellite-based measurement systems such as those conceived as a visionary goal by the ongoing GEOSS and GMES research initiatives.

Manuscript received September 22, 2009; revised May 25, 2010, September 1, 2010, and October 19, 2010; accepted October 31, 2010. Date of publication January 5, 2011; date of current version May 20, 2011.

The author was with the European Commission Joint Research Centre (EC-JRC), 21020 Ispra (Va), Italy. He is now with the Department of Geography, University of Maryland, College Park, MD 20740 USA (e-mail: andrea.baraldi@hermes.geog.umd.edu).

Color versions of one or more of the figures in this paper are available online at <http://ieeexplore.ieee.org>.

Digital Object Identifier 10.1109/TGRS.2010.2091137

Index Terms—Decision-tree classifier, fuzzy-rule-based system, image classification, prior knowledge, radiometric calibration, remote sensing (RS).

I. INTRODUCTION

IN RECENT years, cost-free access to large-scale low-spatial-resolution (SR) (above 40 m) and medium-SR (from 40 to 20 m) spaceborne image databases has become a reality [1]–[3]. In parallel, the demand for high-SR (between 20 and 5 m) and very high SR (VHR, below 5 m) commercial satellite imagery has continued to increase in terms of data quantity and quality, which has boosted the rapid growth of the commercial VHR satellite industry [2].

These multiple drivers make urgent the need to develop operational satellite-based measurement systems suitable for automating the quantitative analysis of large-scale spaceborne multisource multiresolution image databases [1]. This ambitious objective has been traditionally pursued by the remote-sensing (RS) community involved with global land cover (LC) and LC change programs [1, pp. 451, 452]. The same objective is currently envisaged under ongoing international programs such as the Global Earth Observation System of Systems (GEOSS), conceived by the Group on Earth Observations (GEO) [3], and the Global Monitoring for the Environment and Security (GMES), an initiative led by the European Union in partnership with the European Space Agency (ESA) [4].

Unfortunately, the automatic or semiautomatic transformation of huge amounts of multisource multiresolution RS imagery into information still remains far more problematic than might be reasonably expected [5]. This well-known opinion by Zamperoni may explain why, to date, the percentage of data downloaded by stakeholders from the ESA Earth-observation (EO) databases is estimated at about 10% or less.

If productivity in terms of quality, quantity, and value of high-level output products generated from input EO imagery is low, this is tantamount to saying that existing scientific and commercial RS image understanding (classification) systems (RS-IUSs), e.g., [6]–[8], score poorly in operational contexts. This inference would also apply to two-stage segment-based RS-IUSs [6], [8], which have recently gained widespread popularity and whose conceptual foundation is well known in literature as (2-D) object-based image analysis [9].

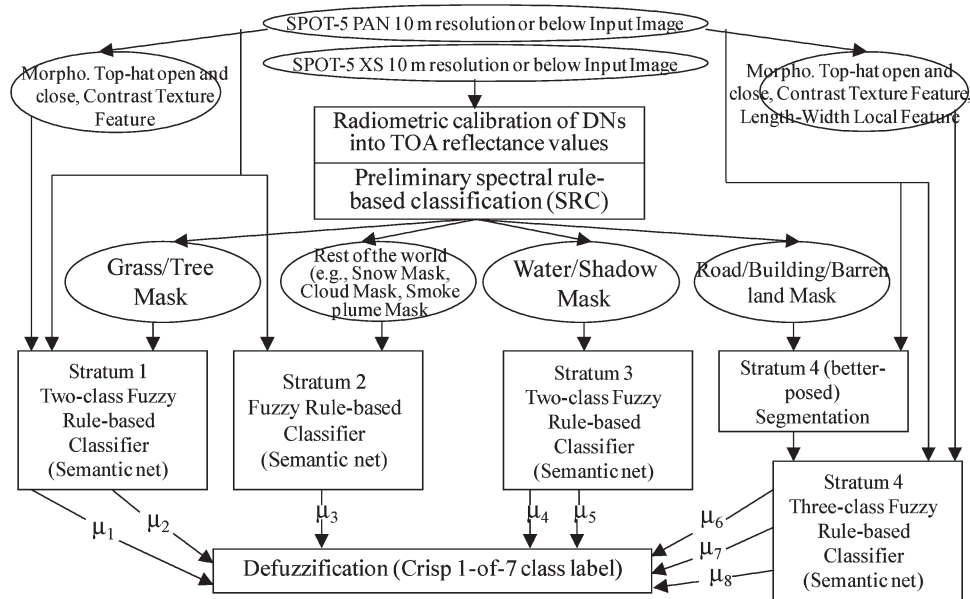


Fig. 1. Novel hybrid two-stage stratified hierarchical RS-IUS architecture. This data flow diagram shows processing blocks as rectangles and sensor-derived data products as circles [26]. In this example, a SPOT-5 MS image is adopted as input. The panchromatic image can be generated from the MS image. The MS image is input to the preliminary classification first stage and, if useful, to the second-stage class-specific classification modules. The panchromatic image is exclusively employed as input to second-stage stratified class-specific context-sensitive classification modules, where color information is dealt with by stratification. For example, stratified texture detection is computed in the panchromatic image domain, which reduces computation time.

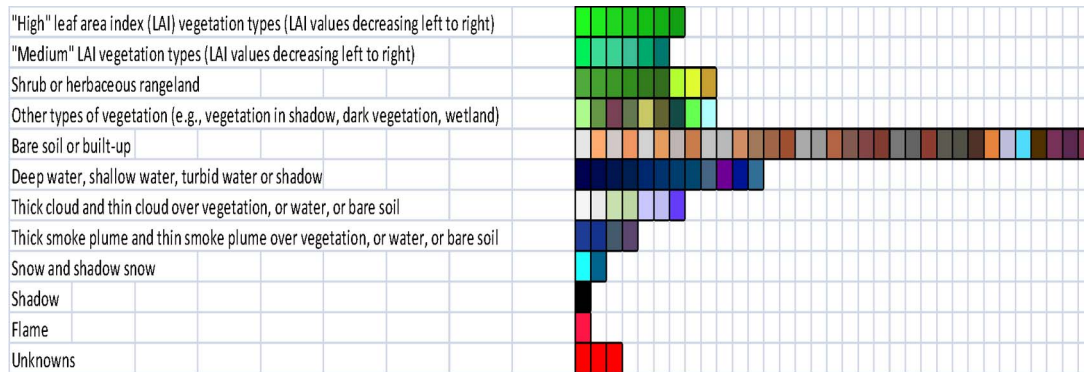


Fig. 2. Preliminary classification map legend adopted by SRC. Pseudocolors associated with spectral categories are gathered based on their spectral end-member (e.g., bare soil or built-up) or parent spectral category (e.g., "high" LAI vegetation). The pseudocolor of a spectral category is chosen as to mimic natural colors of pixels belonging to that spectral category.

To outperform existing scientific and commercial image mapping systems, there is a new trend in both computer vision [10] and RS literature [11], [12]. This trend is focused on the development of hybrid models for retrieving subsymbolic continuous variables [e.g., leaf area index (LAI)] and symbolic categorical discrete variables (e.g., LC composition) from optical multispectral (MS) imagery. By definition, hybrid models combine both statistical (bottom-up, fine-to-coarse, driven-without-knowledge, and inductive-learning-by-example) and physical (top-down, coarse-to-fine, prior-knowledge-based, and deductive-learning-by-rule) models to take advantage of the unique features of each and overcome their shortcomings [10]–[12].

Novel achievements in the development of an operational automatic near-real-time hybrid RS-IUS accomplished by the author of this work were recently published in RS literature [13]–[19]. These new developments encompass the four levels

of analysis of an information processing device, namely: 1) computational theory (architecture); 2) knowledge/information representation; 3) algorithm design; and 4) implementation [19], [20]. Accounting for the customary distinction between a model and the algorithm used to identify it [20], an original two-stage stratified hierarchical hybrid RS-IUS architecture (see Fig. 1) was identified starting from several RS-IUS implementations proposed by Shackelford and Davis in recent years [21], [22]. This novel RS-IUS architecture comprises the following [13]–[19].

- 1) A radiometric calibration preprocessing stage, where digital numbers are transformed into top-of-atmosphere reflectance (TOARF) or surface reflectance (ρ) values, with $TOARF \geq \rho$. This is considered a necessary, although not sufficient, condition for input EO imagery to be understood automatically.

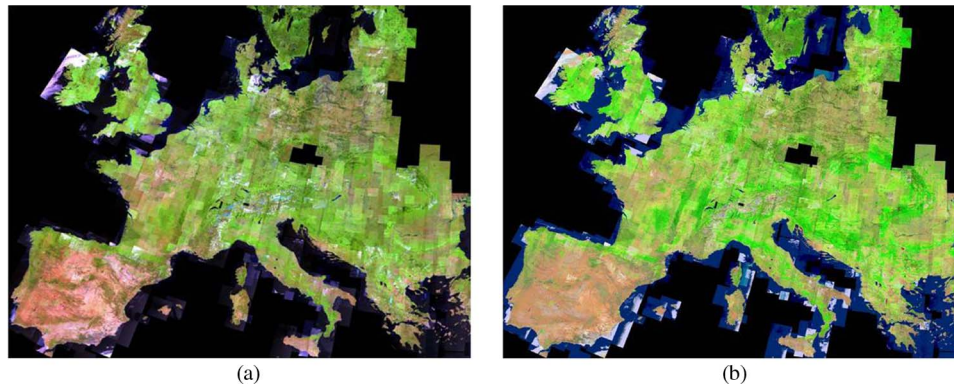


Fig. 3. (a) Four-band GMES-IMAGE2006 Coverage 1 mosaic, consisting of approximately 2000 four-band IRS-1C/-1D/P6 LISS-III, SPOT-4 HRVIR, and SPOT-5 HRG images, mostly acquired during the year 2006, depicted in false colors: (Red) Band 4 (short-wave infrared), (green) Band 3 (NIR), and (blue) Band 1 (visible green). Downscaled SR: 25 m. (b) Preliminary classification map automatically generated by SSRC from the mosaic shown in (a). Output spectral categories are depicted in pseudocolors. Map legend is shown in Fig. 2. This result was achieved at the European Commission-Joint Research Center in October 2008 and published in [13] and [16]. To the best of the author’s knowledge, this is the first example of such a high-level product automatically generated at continental scale at both the European Commission-Joint Research Center facility and elsewhere.

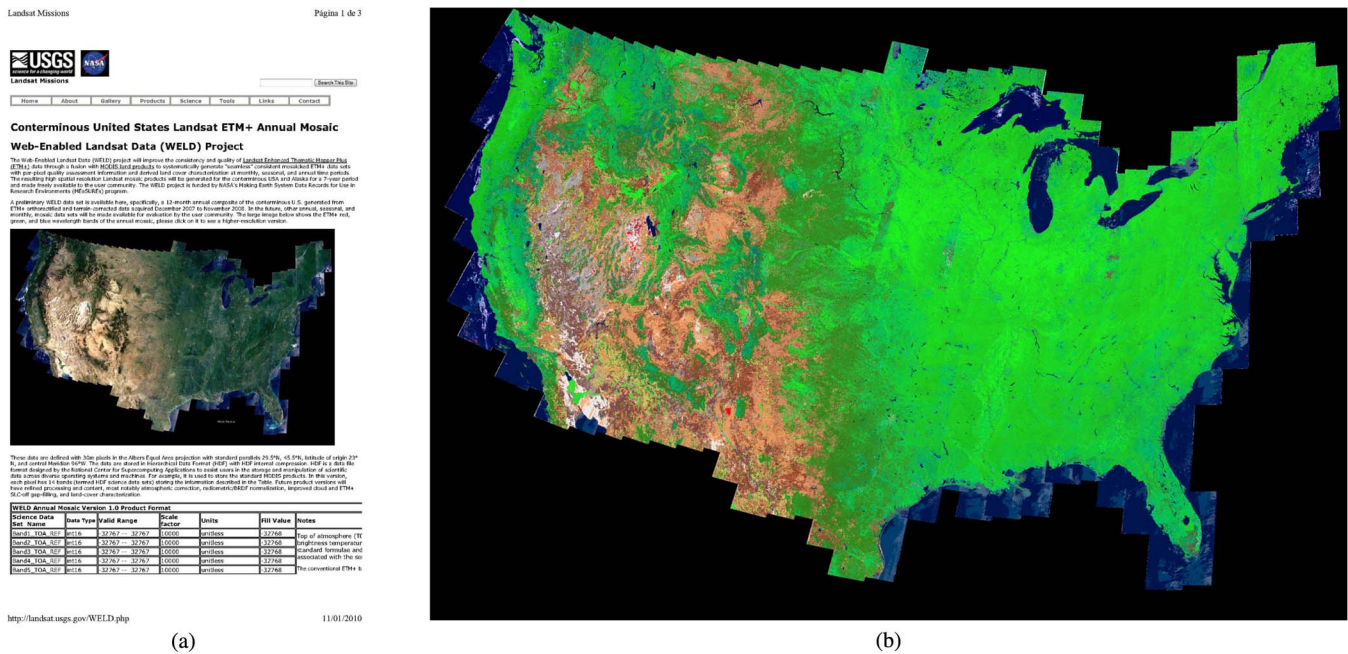


Fig. 4. (a) (Left) Web-enabled Landsat Data Project (<http://landsat.usgs.gov/WELD.php>). This is a joint NASA and USGS project providing seamless consistent mosaics of fused Landsat-7 ETM+ and MODIS data radiometrically calibrated into TOARF and surface reflectance. These mosaics are made freely available to the user community. Each consists of 663 fixed location tiles. SR: 30 m. Area coverage: Continental U.S. and Alaska. Period coverage: Seven years. Product time coverage: Weekly, monthly, seasonal, and annual composites. (b) (Right) Preliminary classification map automatically generated by LSRC from the 2008 annual Web-enabled Landsat Data mosaic shown in (a). Output spectral categories are depicted in pseudocolors. Map legend is shown in Fig. 2. LSRC was run by L. Boschetti (University of Maryland) and Junchang Ju and D. Roy (University of South Dakota) in October 2010. To the best of the author’s knowledge, this is the first example of such a high-level product automatically generated at continental scale at both the NASA and USGS.

- 2) A first-stage application-independent per-pixel (noncontextual) top-down (prior-knowledge-based) preliminary classifier in the Marr sense [20].
- 3) A second-stage battery of stratified hierarchical context-sensitive application-dependent modules for class-specific feature extraction and classification.

The first-stage pixel-based preliminary classifier was designed and implemented as an original operational automatic near-real-time per-pixel multisource multiresolution application-independent spectral-rule-based decision-tree classifier (SRC). In [13]–[19], the coauthors worked independently

of the present author to provide an SRC with an independent scientific scrutiny for validation over a wide range of spatial conditions, time periods, optical imaging sensors, and geographic extents ranging from local to regional and continental scales, e.g., see Figs. 2–4.

To the best of the author’s knowledge, no unifying automatic multisensor multiresolution RS image classification cross-platform alternative to SRC can be found in existing literature. For this reason, this work adopts SRC as a benchmark (reference) classifier and tries to answer the following question: How can the reference SRC first stage of a two-stage hybrid RS-IUS be improved in operational contexts?

To answer this question, it is noteworthy that, for the sake of simplicity, i.e., to reduce its number of free parameters, the original SRC decision-tree formulation adopts crisp (hard) membership functions (MFs) in combination with a hierarchical modular structure to generate as output a sorted set of so-called spectral categories (equivalent to leaves of the decision tree) [14], [15]. In terms of machine learning [23], the crisp SRC decision tree belongs to the family of nonadaptive binary decision trees. In general, nonadaptive decision trees are, first, prespecified, where intuition, domain expertise, and evidence from data are combined by a human expert in an *ad hoc* process to come up with a final mapping of data [23, p. 391], and second, inherently sensitive to changes in hierarchy [23, p. 157].

The well-known conceptual foundation of fuzzy logic [24] appears as a valuable tool capable of improving the operational quality indicators (QIs) (refer to Section II-C) of a crisp SRC decision tree. In particular, the replacement of a crisp SRC with a fuzzy SRC as the first stage of a two-stage stratified hierarchical hybrid RS-IUS is expected to achieve the following operational advantages based on theoretical considerations.

- 1) Provide the first-stage preliminary classification output map (known as primal sketch in the Marr sense [20]) with a superior information/knowledge representation [25], where component cover classes of mixed pixels (class mixture) are modeled (to be properly dealt with at the second stage of the proposed two-stage hybrid RS-IUS architecture). In the words of Wang, “if knowledge representation is poor, even sophisticated algorithms can produce inferior outputs. On the contrary, improvement in representation might achieve twice the benefit with half the effort.”
- 2) Transform the crisp (hierarchical) SRC decision-tree structure into a fuzzy horizontal (flat) SRC system design independent of hierarchy [23, pp. 157, 390]. In operational terms, a crisp-to-fuzzy SRC design transformation means that the fuzzy SRC software features enhanced maintainability/scalability/reusability (refer to Section II-C) [26], [27].

To counterbalance the expected advantages 1) and 2) aforementioned, it is noteworthy that a sequential (single-process single-thread) implementation of the inherently parallel fuzzy SRC is expected to be computationally more intensive than a sequential implementation of the inherently sequential crisp SRC decision tree (where every pixel-based MS data vector activates a single leaf of the decision tree). Fortunately, the computational overload of the fuzzy SRC versus the crisp SRC would reduce to zero if parallel computation (single-process multithread) is adopted instead.

Based on these theoretical considerations, *the objective of this work is to replace the crisp pixel-based preliminary SRC (hierarchical) decision-tree first stage of a two-stage stratified hierarchical hybrid RS-IUS instantiation* (see Fig. 1) *with a fuzzy (horizontal) SRC.*

To better pose the fuzzy SRC system development project and, at the same time, make it more ambitious, this work adopts

additional system requirements. In particular, the fuzzy SRC system is required not to lose any of the operational qualities of the crisp SRC decision tree. Since the crisp SRC performs “well” in operational contexts [13]–[19], then, in addition to modeling class mixture, which is its added value, the fuzzy SRC is required to perform like the crisp SRC in terms of degree of automation, accuracy, robustness, and scalability.

These project requirements provide a set of necessary conditions for validation of the fuzzy SRC. They also mean that, in this work, no absolute accuracy measure of the fuzzy SRC is mandatory. Rather, a relative performance assessment of the fuzzy SRC in comparison with the crisp SRC, employed as a benchmark classifier, is necessary. The interested reader is referred to existing literature for validation of the crisp SRC in the mapping of RS images acquired across time, space, and sensors [13]–[19].

The rest of this paper is organized as follows. In Section II, basic concepts and definitions employed in this work are made explicit. SRC-specific concepts and SRC-related works are reviewed in Section III. In Section IV, the fuzzy SRC system implementation strategy is sketched. An experimental session is selected in Section V. Experimental results are discussed in Section VI. Conclusions are reported in Section VII.

II. BASIC CONCEPTS AND DEFINITIONS

In Section I, the goal of this work is defined as the transformation of an operational automatic nonadaptive (predefined) crisp binary SRC (hierarchical) decision tree into a nonadaptive fuzzy (horizontal) SRC capable of losing none of the operational qualities of the former.

In general, *basic concepts and definitions adopted in this work are not community-agreed and/or tend to be ignored in RS common practice. In this section, they are made explicit to reduce their potential degree of ambiguity and thus contribute to making this paper self-contained.*

A. S- and Z-MFs

In the traditional field of artificial intelligence [23], systems of fuzzy IF–THEN rules consist of a set of simultaneous univariate premises (conditions on scalar input variables) and an output consequence (action), e.g., IF (temperature is low) AND (pressure is high) THEN (ignition value is 0.7). Linguistic terms specifying input and output values are fuzzy sets (FSs) with MFs. FSs in the antecedent (IF) part are called input FSs, and FSs in the consequent (THEN) part of fuzzy rules are called output FSs. By definition [14], an FS_L is an ordered pair $FS_L(x_n) = \{(x_n, \mu_L(x_n)) | \mu_L(x_n) \in [0, 1], x_n \in \mathfrak{R}, n \in \{1, N\}\}$, where N is the sample set size and $\mu_L(x_n)$ is an MF associated with a linguistic label L (e.g., low, medium, and high). An MF maps the scalar input space of real numbers \mathfrak{R} to the bounded nonnegative real membership space $[0, 1]$. In this case, the IF–THEN rule is termed fuzzy. In practice, an FS_L is a class-specific and linguistic label L -specific set of value pairs, $(x_n, \mu_L(x_n))$, possessing a continuum of membership grades, i.e., there is no sharp boundary among x_n elements that belong to this class and those that do not [24]. If the membership space

consists of only two discrete values, equivalent to zero and one, then the IF–THEN rule is not termed fuzzy but is hard or crisp.

Typical examples of fuzzy MFs are the 1-D Gaussian MFs and the S- and Z-MFs. A typical implementation of a fuzzy S-function is the following [28]:

$$\begin{aligned} \mu_{L,S}(x_n) &= S(x_n; a, b, c : a < (b = (a + c)/2) < c) \\ &= \begin{cases} 0, & x_n \leq a \\ 2 \{(x_n - a)/(c - a)\}^2, & a < x_n \leq b, c > a \\ 1 - 2 \{(x_n - c)/(c - a)\}^2, & b < x_n \leq c, c > a \\ 1, & x_n > c. \end{cases} \quad (1) \end{aligned}$$

This S-function is controlled by the two free parameters a and c . The derived variable $b = (a + c)/2$ denotes the *crossover point*, where $\mu_{L,S}(b) = 0.5$. The *bandwidth* parameter Δb of the S-function is defined as $0 < \Delta b = b - a = c - b$. The Z-function is derived from the S-function as follows:

$$\begin{aligned} \mu_{L,Z}(x_n) &= Z(x_n; a, b, c) \\ &= 1 - S(x_n; a, b, c : a < b = (a + c)/2 < c). \quad (2) \end{aligned}$$

In the crisp instantiation of the S- and Z-functions, parameters a and c of (1) and (2) tend to coincide, i.e., $a \rightarrow b = [(a + c)/2] = Th \rightarrow c$, then $\Delta b \rightarrow 0$. In this case, the crisp version of (1) becomes $\mu_{L,S}(x_n) = S(x_n; Th) = \{0 \text{ if } x_n \leq Th \text{ OR } (1 \text{ if } x_n > Th)\}$.

B. Absolute Radiometric Calibration Into TOARF Values

As reported in Section I, SRC requires as input an MS image radiometrically calibrated into TOARF or surface reflectance (ρ) values, the latter being an ideal (atmospheric noise-free) case of the former, i.e., $TOARF \supseteq \rho$ [13]–[19]. This allows SRC to consider the inherently ill-posed atmospheric correction preprocessing of an input MS image optional rather than compulsory. It also means that SRC must employ as input MS imagery provided with radiometric calibration metadata files.

Table I reports on the relationship existing between commercial RS-IUSs and the radiometric calibration constraint considered mandatory by the international Quality Assurance Framework for EO (QA4EO) [38] delivered by the Working Group on Calibration and Validation of the Committee of Earth Observations (CEOS), the space arm of GEO [3]. Table I shows that, first, no existing commercial RS-IUS software, except for the ERDAS ATCOR3 software module [7], requires radiometric calibration preprocessing. In recent papers, the present author highlighted the fact that by making RS data well behaved and well understood, *radiometric calibration* not only ensures the harmonization and interoperability of multisource observational data according to the QA4EO guidelines [38] but *is also a necessary, although insufficient, condition for automating the quantitative analysis of EO data* [13]–[19]. This necessary condition for automatic EO data interpretation agrees with common sense, summarized by the expression “garbage in, garbage out.” In the terminology of machine learning and

TABLE I
EXISTING COMMERCIAL RS-IUSs AND THEIR DEGREE OF MATCH WITH THE INTERNATIONAL QA4EO GUIDELINES

Commercial RS-IUSs	Sub-symbolic (asemantic) versus symbolic (semantic) information primitives, namely, pixels / (2-D) objects (regions, segments) / strata	Radiometric calibration (RAD. CAL.) requirement according to the international QA4EO guidelines
PCI Geomatics GeomaticaX	Sub-symbolic pixels	NO RAD. CAL. \Rightarrow semi-automatic and site-specific
eCognition Server by Definiens AG	Unsupervised data learning sub-symbolic objects	NO RAD. CAL. \Rightarrow semi-automatic and site-specific
Pixel- and Segment-based versions of the Environment for Visualizing Images (ENVI) by ITT VIS	Either sub-symbolic pixels or unsupervised data learning sub-symbolic objects	NO RAD. CAL. \Rightarrow semi-automatic and site-specific
ERDAS IMAGING Objective	Supervised data learning symbolic objects	NO RAD. CAL. \Rightarrow semi-automatic and site-specific
ERDAS Atmospheric Correction-3 (ATCOR3)	Sub-symbolic pixels	Consistent with the QA4EO: surface reflectance, $\rho \Rightarrow$ inherently ill-posed atmospheric correction first stage \Rightarrow semi-automatic and site-specific.
Novel two-stage stratified hierarchical RS-IUS employing SRC as its preliminary classification first stage	Prior knowledge-based symbolic pixels \in symbolic objects \in symbolic strata	Consistent with the QA4EO: top-of-atmosphere (TOA) reflectance (TOARF) or surface reflectance ρ values, with TOARF $\supseteq \rho \Rightarrow$ atmospheric correction is optional. Automatic and robust to changes in RS optical imagery acquired across time, space and sensor.

computer vision, the radiometric calibration constraint augments the degree of prior knowledge of an RS-IUS required to complement the intrinsic insufficiency (ill-posedness) of (2-D) image features, i.e., radiometric calibration makes the inherently ill-posed computer vision problem better posed.

To summarize, in disagreement with the QA4EO guidelines, most existing scientific and commercial RS-IUSs, such as those listed in Table I, do not require RS images to be radiometrically calibrated and validated. As a consequence, according to the aforementioned necessary condition for automating the quantitative analysis of EO data, these RS-IUSs are semiautomatic and/or site specific (since one scene may represent, for example, apples, while any other scene, even if contiguous or overlapping, may represent, for example, oranges) (refer to Table I). Second, Table I shows that, unlike SRC, the ERDAS ATCOR3 requires as input an MS image radiometrically calibrated into surface reflectance ρ values exclusively. This implies that the ERDAS ATCOR3 software considers mandatory the inherently ill-posed and difficult-to-solve MS image atmospheric correction preprocessing stage which requires user intervention to make it better posed [7]. Thus, unlike SRC, the ERDAS ATCOR3 satisfies the necessary condition for automating the quantitative analysis of EO data, but is insufficient to provide an RS image classification problem with an automatic workflow requiring no empirical parameter to be user defined based on heuristic criteria.

C. Operational QIs of an RS-IUS

In operational contexts, an RS-IUS is defined as a low performer if at least one among several operational QIs¹ scores low. Typical operational qualities of an RS-IUS encompass the following [26], [27].

- 1) Degree of automation. For example, a data processing system is *automatic* when it requires no user-defined parameter to run; therefore, its user-friendliness cannot be surpassed. When a data processing system requires neither user-defined parameters nor reference data samples to run, then it is termed “*fully automatic*” [35]. Section II-B reports that radiometric calibration is a necessary, although insufficient, condition for automating the quantitative analysis of EO data [13]–[19].
- 2) Effectiveness, e.g., classification accuracy.
- 3) Efficiency, e.g., computation time, memory occupation, etc.
- 4) Economy (costs). For example, open-source solutions are welcome to reduce costs of software licenses.
- 5) Robustness to changes in the input data set, e.g., changes due to noise in the data.
- 6) Robustness to changes in input parameters, if any.
- 7) Maintainability/scalability/reusability to keep up with changes in users’ needs and sensor properties.
- 8) Timeliness, defined as the time span between data acquisition and product delivery to the end user. It increases monotonically with manpower, e.g., the manpower required to collect site-specific training samples.

The aforementioned list of operational QIs is neither irrelevant nor obvious. For example, a low score in operational QIs may explain why the literally hundreds of so-called novel low-level (subsymbolic) and high-level (symbolic) image processing algorithms presented each year in scientific literature typically have a negligible impact on commercial RS image processing software [5]. This conjecture is consistent with the fact that most works published in RS literature assess and compare spaceborne image classification algorithms in terms of mapping accuracy exclusively, which corresponds to the sole operational performance indicator 2) listed earlier. Moreover, these classification accuracy estimates are rarely provided with a degree of uncertainty in measurement [as a negative example not to be imitated (see [36])]. This violates well-known laws of sample statistics [29], [30], [37], together with

¹Any evaluation measure is inherently noninjective [17]. For example, in classification-map accuracy assessment and comparison, different classification maps may produce the same confusion matrix while different confusion matrices may generate the same confusion matrix accuracy measure, such as the overall accuracy (OA). These observations suggest that no single universally acceptable measure of quality, but instead a variety of quality indices, should be employed in practice [29], [30]. To date, this general conclusion is neither obvious nor community-agreed. For example, in computer vision and RS, this conclusion implies that when a test image and a reference (original) image pair is given, common attempts to identify a unique (universal) reliable image quality index, such as the relative dimensionless global error ERGAS proposed in [31], the universal image quality index Q [32], the global image quality measure Q4 [33], and the quality index with no reference QNR [34], are inherently undermined as contradictions in terms.

common sense envisaged under the international guidelines of the QA4EO. In particular, the QA4EO guidelines require that *every sensor-derived data product, generated across a satellite-based measurement system’s processing chain, be provided with metrological/statistically based QIs featuring a degree of uncertainty in measurement* [38].

To summarize, the operational quality assessment of many RS-IUSs presented in literature does not satisfy the international QA4EO recommendations. In practice, operational qualities of published RS-IUSs remain largely unknown. Based on the evidence that these RS-IUSs have had a negligible impact on commercial and scientific RS image processing software toolboxes, the conclusion is that these RS-IUSs are expected to score poorly in operational contexts.

D. Crisp Classification Accuracy Measures and Confidence Interval

Section II-C mentions that, in violation of common sense and sample statistics envisaged under the GEO-CEOS international QA4EO guidelines, most works published in RS literature assess and compare alternative spaceborne image classification algorithms exclusively in terms of mapping accuracy provided with no confidence interval.

According to sample statistics, it is well known that any classification OA probability estimate $p_{OA} \in [0, 1]$ is a random variable (sample statistic) with a confidence interval (error tolerance) $\pm\delta$ associated with it, where $0 < \delta < p_{OA} \leq 1$ [29], [30], [37]. In other words, $p_{OA} \pm \delta$ is a function of the specific test data set used for its estimation and vice versa [37]. For example, given a target classification accuracy probability p_{OA} and a test sample set size M_{test} comprising independent and identically distributed reference samples (in RS common practice, this hypothesis is often violated due to spatial autocorrelation between neighboring pixels selected as reference samples), the half width δ of the error tolerance $\pm\delta$ at a desired confidence level (e.g., if confidence level = 95%, then the critical value is 1.96) can be computed as follows [29], [37], [39]:

$$\delta = \sqrt{\frac{(1.96)^2 \cdot p_{OA} \cdot (1 - p_{OA})}{M_{\text{test}}}}. \quad (3)$$

For each c th class simultaneously involved in the classification process, with $c = 1, \dots, C$, where C is the total number of classes, it is possible to prove that (refer to [42, p. 294])

$$\delta_c = \sqrt{\frac{\chi_{(1,1-\alpha/C)}^2 \cdot p_{OA,c} \cdot (1 - p_{OA,c})}{m_{\text{test},c}}}, \quad c = 1, \dots, C \quad (4)$$

where α is the desired level of significance, i.e., the risk that the actual error is larger than δ_c (e.g., $\alpha = 0.07$), $(1 - \alpha/C)$ is the level of confidence, and $\chi_{(1,1-\alpha/C)}^2$ is the upper $(1 - \alpha/C) * 100$ th percentile of the chi-square distribution with 1 DOF. For example, if $\alpha = 0.04$ and $C = 4$, then the level of confidence is $(1 - 0.04/4) = 0.99$, and then, $\chi_{(1,0.99)}^2 = 6.63$.

Starting from (4), the class-specific training data set cardinality, $m_{\text{test},c}$, with $c = 1, \dots, C$, required for target δ_c , $p_{\text{OA},c}$, and α parameters becomes

$$m_{\text{test},c} = \frac{\chi_{(1,1-\alpha/C)}^2 \cdot p_{\text{OA},c} \cdot (1 - p_{\text{OA},c})}{\delta_c^2}, \quad c = 1, \dots, C. \quad (5)$$

Typical values of classification accuracy and confidence interval are employed as a benchmark by the RS community. The target OA $p_{\text{OA}} \in [0, 1] \pm \delta = (3)$ is fixed at $0.85 \pm 2\%$, in agreement with the U.S. Geological Survey (USGS) classification system constraints [40]. The class-specific classification accuracies $p_{\text{OA},c} \in [0, 1] \pm \delta_c = (4)$, $c = 1, \dots, C$, should be about equal to, and never below, 70% [31], whereas a reasonable reference standard for δ_c is about 5%.

In this paper (see Section V-D), the test data set consists of reference samples belonging to four target spectral categories (equivalent to LC class sets; refer to Section III below and [15]), namely, “either woody vegetation or cropland or grassland,” “rangeland,” “either bare soil or built-up,” and “water”; thus, $C = 4$ (refer to Section V-D). Since $C = 4$, if $\alpha = 0.04$, then $(1 - \alpha/C) = 0.99$, and $\chi_{(1,0.99)}^2 = 6.63$ (refer to previous discussion). If δ_c is set equal to 5% and the target $p_{\text{OA},c} = 85\%$, then the required cardinality of class-specific reference samples becomes $m_{\text{test},c} = (5) \approx 340$, $c = 1, \dots, 4$.

E. Fuzzy Classification Accuracy Measures

One additional advantage of using “soft” classifiers, as opposed to “hard” ones, is that the former provide the possibility of using many measures for accuracy assessment of a classification beyond the standard $p_{\text{OA}} \in [0, 1]$ and confusion matrix [29], [39]. A number of approaches are available, e.g., fuzzy operators [41], fuzzy distances and the Shannon entropy [42], the index of fuzziness [43], the fuzzy OA (FOA) [44], several measures of fuzzy similarity [45], and the fuzzy error matrix, which is a generalization of the standard confusion matrix and provides several indicators of classification accuracy such as the FOA and, for each category, the producer’s accuracy and the user’s accuracy [44].

In this paper, the fuzzy output of the proposed fuzzy SRC is not evaluated by any of the fuzzy accuracy measures mentioned above before “hardening” occurs. The reason is that no pixel-based ground-truth contribution of each category in the selected set of test images was available (see Section V-D). As a matter of fact, class mixture information would be very tedious, expensive, and difficult to acquire based on field sites, existing maps, and tabular data; indeed, class mixture ground truth is almost never available in practice.

Considering that this paper is focused on a relative assessment of the fuzzy SRC in comparison to the crisp SRC rather than on an absolute validation of the former (refer to Section I), the absence of a reference data set providing ground-truth contributions to mixed pixels can be overcome by the comparison of the reference crisp SRC output map with the “hardened” (defuzzified) version of the fuzzy SRC output map, where “multiple winners” (see Section IV-F) are resolved (defuzzified), i.e., they are assigned to one of the best matching spectral categories.

III. SRC-SPECIFIC CONCEPTS AND SRC-RELATED WORKS IN RS IMAGE CLASSIFICATION

As stated in Section I, this work aims at improving the operational QIs of the first automatic multisensor multiresolution hybrid RS-IUS proposed in [13]–[19]. A well-known book on the development of hybrid RS-IUS is, for example, [11]. In RS journals, aside from classic publications such as [25], [46], and [47], few recent papers deal with the machine learning algorithms of potential interest to this work, such as the following.

- 1) Adaptive decision trees, such as the well-known classification and regression binary decision-tree algorithm CART, taken from machine learning [23].
- 2) Nonadaptive decision trees, like SRC [13]–[19].
- 3) Adaptive fuzzy-rule-based systems [48], which require a reference data set which is typically scene specific, expensive, tedious, and difficult or impossible to collect [1].
- 4) Nonadaptive fuzzy-rule-based systems [21], [22], [49], [50], whose tuning is accomplished by a human expert relying on his/her intuition, domain expertise, and evidence from data observation [23]. For example, in [50], FSs employed in fuzzy rules model the size and contrast of image structures investigated via the multiscale differential morphological profile [51].
- 5) Semantic nets, either directed or nonoriented, either cyclic or acyclic, consisting of nodes (representing concepts, i.e., classes of objects in the world) linked by edges (representing relations, e.g., PART-OF, A-KIND-OF, spatial relations, temporal transitions, etc.) between nodes [11], [52]–[54].

Semantic nets deal with the attentive vision phase [55]–[58]; as a consequence, they cope with the *artificial and intrinsic insufficiency of (2-D) image informational primitives* extracted by preattentive vision² [11], [15]–[17]. In other words, in semantic nets, there is no attempt to reduce the part of ill-posedness of the computer vision problem due to the *artificial insufficiency* of image primitives (rather, this reduction is

²The main role of a biological or artificial visual system is to backproject the information in the (2-D) image domain to that in the (3-D) scene domain [11]. In greater detail, the goal of a visual system is to provide plausible (multiple) symbolic description(s) of the scene depicted in an image by finding associations between subsymbolic (2-D) image features with symbolic (3-D) objects (concepts) in the scene (e.g., a building, a road, etc.). Subsymbolic (2-D) image features are either points or regions or, vice versa, region boundaries, i.e., edges, provided with no semantic meaning. In literature, (2-D) image regions are also called segments, (2-D) objects, patches, parcels, or blobs.

There is a well-known information gap between symbolic information in the (3-D) scene and subsymbolic information in the (2-D) image (e.g., due to dimensionality reduction and occlusion phenomena). This is called the *intrinsic insufficiency* of image features. It means that the problem of image understanding is inherently ill-posed and, consequently, very difficult to solve [11], [15].

In functional terms, biological vision combines preattentive (low-level) visual perception with an attentive (high-level) vision mechanism [55]–[57].

1) Preattentive (low-level) vision extracts picture primitives based on general-purpose image processing criteria independent of the scene under analysis. It acts in parallel on the entire image as a rapid (< 50 ms) scanning system to detect variations in simple visual properties. It is known that the human visual system employs at least four spatial scales of analysis [58].

2) Attentive (high-level) vision operates as a careful scanning system employing a focus of attention mechanism. Scene subsets, corresponding to a narrow aperture of attention, are looked at in sequence and each step is examined quickly (20–80 ms).

exactly the objective of the SRC first stage in a two-stage hybrid RS-IUS [15]–[17]). To date, semantic nets lack flexibility and scalability, i.e., they are unsuitable for commercial RS image processing software toolboxes and remain limited to scientific applications.

About SRC, it is noteworthy that, although it belongs to the class of nonadaptive decision trees (see earlier discussion), it was not conceived as a stand-alone classifier; rather, SRC is to be employed as the first stage of a two-stage stratified hierarchical hybrid RS-IUS. As stated in Section I, the degree of novelty of a two-stage stratified hierarchical hybrid RS-IUS provided with a first-stage operational automatic SRC decision tree [13]–[19] (see Fig. 1) encompasses the four levels of analysis of an RS-IUS [19], [20]. Original SRC-specific concepts, definitions, and properties to be recalled in the design Section IV and experiment Section V are summarized hereafter.

The core definition introduced by SRC is that of *spectral-based semiconcept* or *spectral category* or *LC class set* or *spectral end member* [15]. A spectral category is equivalent to a semantic conjecture based exclusively on spectral (i.e., chromatic and achromatic) properties. Spectral properties are inherently noncontextual, i.e., pixel based. For example, one pixel is red like a brick no matter what the colors of its neighboring pixels are. From a spaceborne MS image employed as input, SRC automatically generates as output a *preliminary map* or *primal sketch* in the Marr sense (refer to Section I) [20]. A preliminary SRC map consists of six spectral supercategories (spectral end members), namely: 1) “clouds” (CL); 2) “either snow or ice” (SN); 3) “either water or shadow” (WASH); 4) “vegetation” (V), equivalent to “either woody vegetation or cropland or grassland or (shrub and brush) rangeland”; 5) “either bare soil or built-up” (BB); and 6) “outliers.”³ Spectral supercategories are mutually exclusive and totally exhaustive, in line with the Congalton definition of a classification scheme [29]. Spectral supercategories can split into several subcategories [14]. In the words of Di Gregorio and Jansen [60], although it generates a large number of spectral subcategories, SRC consists of a small number of classification modules of spectral supercategories.

SRC is an operational automatic system of systems, in line with the visionary goal of a GEOSS [3]. It comprises a master seven-band Landsat-like SRC (LSRC) [14] plus five downscaled LSRC subsystems whose spectral resolution overlaps with, but is inferior to, Landsat’s [15]. These downscaled LSRC subsystems are identified as follows: 1) the four-band SPOT-like SRC (SSRC); 2) the four-band Advanced Very High Resolution Radiometer (AVHRR)-like SRC (AVSRC); 3) the five-band ENVISAT Advanced Along-Track Scanning Radiometer-like SRC (AASRC); 4) the four-band IKONOS-like SRC (ISRC); and 5) the three-band Disaster Monitoring Constellation-like SRC (DSRC). As input, SRC requires a radiometrically calibrated MS image acquired by almost any of the ongoing or future planned satellite optical missions (refer to Table II).

³The adopted LC nomenclature is based on the USGS classification hierarchy [59], the Coordination of Information on the Environment, the Food and Agriculture Organization of the United Nations (FAO) Land Cover Classification System [60], and the International Geosphere–Biosphere Programme LC units [49].

For a complete discussion of these subjects, the interested reader is referred to [13]–[19].

IV. PROPOSED CRISP-TO-FUZZY SRC SYSTEM ADAPTATION

Starting from the problem and opportunity recognition proposed in Section I, namely, the fuzzification of the original SRC system of systems presented in [14] and [15], the goal of this paper can be reformulated in mathematical terms.

A. Fuzzy SRC MF

The original SRC, employed as a reference (see Section I), adopts crisp S- and Z-functions parameterized by a crisp threshold $Th \in \mathfrak{R}_0^+$ found in [14, Tab. III] (see Section II-A). These crisp MFs should be replaced by fuzzy S- and Z-MFs, namely, (4) and (5), respectively, controlled by the parameter pair $a < c$, such that $a = f_1(Th) < b = [(a + c)/2] = Th \in \mathfrak{R}_0^+ < c = f_2(Th)$, with $f_1(\cdot) \neq f_2(\cdot)$, where $b = Th$ is the *crossover point* such that $\mu_{L,S}(Th) = 0.5$, with bandwidth $0 < \Delta b = b - a = c - b$ (see Section II-A). Obviously, if the fuzzy S- and Z-function bandwidth $\Delta b \rightarrow 0$, i.e., if $a \rightarrow b = Th \rightarrow c$, then the fuzzy and the crisp SRC are expected to perform in the same way. This simple observation provides a useful criterion in validating the fuzzy SRC implementation against theory.

B. Fuzzy SRC Data Coding

The bounded nonnegative real membership space $[0, 1]$ is byte coded, i.e., it is discretized into range $\{0, 255\}$ to reduce dynamic/hard-disk memory occupation of membership values whose discretization error is $1/255 = 0.4\%$.

C. Fuzzy SRC Operators

In [14, Tab. VII], where a hierarchy of logical expressions generates a set of Boolean spectral categories, the Boolean-AND operator is replaced by the fuzzy-AND (minimum), the Boolean-OR operator is replaced by the fuzzy-OR (maximum), and the unary Boolean-NOT(x) operator of the Boolean variable $x \in \{0, 1\}$ is replaced by operator (255- X), with byte-coded membership value $X \in \{0, 255\}$. For more details about information combination operators, refer to [66].

D. Fuzzy SRC Software Architecture

- 1) In line with the Congalton definition of a classification scheme [29], the crisp SRC decision tree provides a mutually exclusive and totally exhaustive mapping of the input image into a discrete and finite set of spectral categories including class “unknown” (outliers) [14], [40] (refer to Section III). In the original (L)SRC decision tree proposed in [14], mutual exclusiveness of spectral categories is guaranteed by a combination of (crisp) MFs with their order of presentation. The prior knowledge of this order of presentation is embedded in the hierarchical structure of a decision tree [23], [61]. This modular hierarchy

TABLE II
SRC SYSTEM OF SYSTEMS: LIST OF SPACEBORNE OPTICAL IMAGING SENSORS ELIGIBLE FOR USE

Legenda. Y: Yes, N: No, C: Complete, I: Incomplete (radiometric calibration offset parameters are set to zero), (E)TM: (Enhanced) Thematic Mapper, B: Blue, G: Green, R: Red, NIR: Near Infra-Red, MIR: Medium IR, TIR: Thermal IR, SR: Spatial Resolution, Pan: Panchromatic. Blue columns: visible channels typical of water and haze. Green column: NIR band typical of vegetation. Brown columns: MIR channels characteristics of bare soils. Red column: TIR channel.												
SRC system of systems		B – (E)TM1, 0.45-0.52 (μm)	G – (E)TM2, 0.52-0.60 (μm)	R – (E)TM3, 0.63-0.69 (μm)	NIR – (E)TM4, 0.76-0.90 (μm)	MIR1 – (E)TM5, 1.55-1.75 (μm)	MIR2 – (E)TM7, 2.08-2.35 (μm)	TIR – (E)TM6, 10.4-12.5 (μm)	SR (m)	Rad. Cal. Y/N, C/I	Pan SR (m)	Notes
LSRC (46 Sp. Cat.)	Landsat-4/-5 TM	×	×	×	×	×	×	×	30	Y-C		Refer to Table I in [15].
	Landsat-7 ETM+	×	×	×	×	×	×	×	30	Y-C	15	Same as above.
	MODIS	×	×	×	×	×	×	×	250, 500, 1000	Y-C		Same as above.
	ASTER		×	×	×	×	×	×	15-30	Y-C		Same as above.
	CBERS-2B	×	×	×	×	×	×	×		N		
SSRC (32 Sp. Cat.)	SPOT-4 HRVIR		×	×	×	×			20	Y-I	10	Refer to Table II in [15].
	SPOT-5 HRG		×	×	×	×			10	Y-I	2.5 - 5	Same as above.
	SPOT-4/-5 VMI		×	×	×	×			1100	Y-I		Same as above.
	IRS-1C/-1D LISS-III		×	×	×	×			23.5	Y-I		
	IRS-P6 LISS-III		×	×	×	×			23.5	Y-I		
	IRS-P6 AWiFS		×	×	×	×			56	Y-I		
AVSRC (39 Sp. Cat.)	NOAA AVHRR			×	×	×		×	1100	Y		Refer to Table II in [15].
	MSG			×	×	×		×	3000	Y		Same as above.
AASRC (39 Sp. Cat.)	ENVISAT AATSR		×	×	×	×		×	1000	Y		Same as above.
	ERS-2 ATSR-2		×	×	×	×		×	1000	Y		
ISRC (25 Sp. Cat.)	IKONOS-2	×	×	×	×				4	Y	1	
	QuickBird-2	×	×	×	×				2.4	Y	0.61	
	GeoEye-1	×	×	×	×				1.64	Y	0.41	
	OrbView-3	×	×	×	×				4	Y	1	
	RapidEye-1 to -5	×	×	×	×				6.5	Y-I		
	ALOS AVNIR-2	×	×	×	×				10	Y		
	KOMPSAT-2	×	×	×	×				4	N	1	
	TopSat	×	×	×	×				5	N	2.5	
	FORMOSA T-2	×	×	×	×				8	N	2	
DSRC (25 Sp. Cat.)	Landsat-1/-2/-3/-4/-5 MSS		×	×	×				79	Y		
	IRS-P6 LISS-IV		×	×	×				5.8	Y-I		
	SPOT-1/-2/-3 HRV		×	×	×				20	Y-I	10	
	DMC		×	×	×				22-32	N		

of crisp MFs is flattened in a fuzzy-rule-based system independent of hierarchy [23], called fuzzy SRC, where first, fuzzy MFs are computed in parallel (horizontally, with the same level of priority) and, second, membership

values are defuzzified (refer to Section I and the following discussion).

2) In the crisp SRC implementation, input data vectors that fall outside the (hyperdimensional) domain of activation

of every spectral category are assigned to class “*unknown*” [14]. In the fuzzy SRC instantiation, outliers are detected when the membership value of the winning spectral category falls below a system threshold parameter to be user defined based on heuristics. Since this threshold identifies the minimum normalized membership value considered acceptable by the user, this threshold parameter features an intuitive physical meaning. Therefore, it is easy to select (by default, it is set equal to 0.2, i.e., pixels whose maximum membership is below 0.2 are assigned to class “*unknown*”).

- 3) A defuzzification stage is built (e.g., in Fig. 1, a defuzzification stage is visible at the output of the second stage of the two-stage hybrid RS-IUS). For every pixel, the winning spectral category is the one featuring the highest membership value (i.e., defuzzification adopts a fuzzy OR operator). If multiple winners exist for a given pixel, then an empirical strategy can be chosen to select one winning category among eligible cowinners (see following discussions).

E. Fuzzy SRC-Specific Output Products

To deal with mixed pixels featuring a class mixture, three original output products are generated by the fuzzy SRC in addition to those generated by the crisp SRC.

- 1) The first fuzzy SRC-specific output product is a continuous maximum membership (MMB) value image in range $[0, 1]$ discretized into byte-coded values $\{0, 255\}$. The fuzzy membership value of pixels belonging to class “*outliers*” (unknown) is conventionally set to zero in the MMB output image.
- 2) The second fuzzy SRC-specific output product is an integer image, called multiple winner counter (MWC), with $MWC \geq 1$. It provides the number of winners pertaining to any pixel such that, at the end of the classification process, $MWC \geq 1$ is image-wide; in fact, since SRC provides a totally exhaustive mapping of the input image (see Section III), then each pixel is mapped onto at least one spectral category, including class “*unknown*.” Pixels featuring multiple winners, such that $(MWC > 1)$, can be mapped onto a special binary mask to be considered with special attention. For example, each pixel featuring $(MWC > 1)$ can be defuzzified, i.e., assigned to one spectral category selected from its list of multiple winners, based on arbitrary user-defined application-specific criteria. Since symbolic spectral categories [e.g., “*vegetation*,” “*clouds*,” etc., (refer to Section III)] are easy to understand by both RS experts and nonexpert users who are naturally familiar with symbolic reasoning, empirical defuzzification criteria for pixels featuring $(MWC > 1)$ are easy (intuitive) to define. For example, a mixed pixel belonging to a (3-D) LC class *wetland*, features multiple winners at primal sketch, for example, spectral categories “*vegetation*” and “*either water or shadow*”; between these two winning spectral categories, that pixel is arbitrarily assigned to the former by the defuzzification strategy.

- 3) The third fuzzy SRC-specific output product is a binary map called mixed pixel mask (MPM) $\in \{0, 1\} = \{\text{False}, \text{True}\}$, where False = 0 and True = 1. It identifies pixels for which the difference between the best membership and the second best membership is smaller than a given threshold $\alpha \in [0, 1]$ (by default, $\alpha = 0.2$). These are pixels whose second best membership value is considered “close enough” to the winning (largest) membership value to be considered mixed pixels. These mixed pixels include pixels affected by multiple winners, i.e., $(MPM \text{ EQ True}) \supseteq (MWC > 1) \forall \alpha \geq 0$. If $\alpha = 0$, then relationship $(MPM \text{ EQ True}) == (MWC > 1)$ must hold. These two relationships provide a useful debugging tool in verifying the adequacy of the fuzzy SRC implementation against theory (refer to Section V-C1).

F. Adopted Terminology

For the sake of simplicity, the following terminology is adopted. Pixels belonging to the binary mask $(MWC > 1)$ are called multiple winners. Pixels belonging to the binary mask $(MPM \text{ EQ True})$ are identified as “mixed pixels,” such that $(MPM \text{ EQ True}) \supseteq (MWC > 1)$.

To summarize, at the second stage of a two-stage stratified hierarchical hybrid RS-IUS whose pixel-based preliminary classification first stage is the fuzzy SRC (see Fig. 1), multiple winners, for which condition $(MWC > 1)$ holds, should be handled with special attention. They represent the worst case within the set of mixed pixels $(MPM \text{ EQ True}) \supseteq (MWC > 1) \forall \alpha \geq 0$.

V. EXPERIMENTAL SESSION DESIGN

To provide a quantitative validation of the novel fuzzy SRC, the Prechelt test session criteria [62] are integrated with experimental constraints found in [17] and [63]. These experimental session design criteria are summarized next.

- 1) To test the robustness of a novel approach to changes in the input data set, select at least two real and/or standard/appropriate data sets. For example, a typical standard/appropriate data set is a synthetic data set of standard quality whose signal-to-noise ratio is known and controlled by the user.
- 2) Based on [63], a set of RS images suitable for comparing the performance of alternative algorithms should have the following characteristics: 1) consistent with the aim of testing; 2) as realistic as possible, i.e., each member of the set should reflect a given type of images encountered in practice; and 3) mutually uncorrelated, to reduce the cardinality of the test data set.
- 3) Employ a battery of measures of success [QIs (refer to Section II-C)] capable of dealing with the well-known noninjective property of any quality index (refer to footnote 1) [17].
- 4) For comparison purposes, select at least one alternative existing well-known approach as a benchmark, e.g., in our case, the crisp SRC is employed as a reference (see Section I).

The aforementioned experimental session quality criteria are satisfied as described next.

A. Selection of Competing Classifiers

The four fuzzy LSRC, SSRC, AVSRC, and ISRC subsystems of the integrated fuzzy SRC system of systems (refer to Section III) are quantitatively compared against their crisp counterparts employed as a reference (refer to Section I). In this comparison, the SRC subsystems AASRC and DSRC are omitted to reduce the paper length without losing any meaningful information. AASRC and DSRC differ from AVSRC and ISRC, respectively, by a single band in the visible portion of the electromagnetic spectrum (see Table II). However, SRC assigns slight importance (low weight) to evidence collected from visible bands in its multiple-criteria decision-making process (so as not to be very sensitive to haze and atmospheric effects [14]–[17]). This means that output maps of AASRC and DSRC are very similar to (i.e., highly correlated with) those of AVSRC and ISRC, respectively (typically, these map pair correlation values are greater than 0.9 when synthetic images are employed as input).

B. Selection of the Test Image Set

Three real-world Landsat images are selected to depict a variety of natural and anthropogenic landscapes at different geographic footprints and acquisition times. Next, the selected Landsat images are radiometrically calibrated into TOARF values [13]–[19]. Finally, to make result assessment and comparison easier for a domain expert, one test subimage is selected from each radiometrically calibrated seven-band Landsat image. The three test subimages are as follows: 1) a Landsat-7 Enhanced TM Plus (ETM+) subimage of the city area of Bologna, Italy, 434 (lines) \times 400 (columns) pixels in size, path: 192, row: 029, acquisition date: June 20, 2000 [see Fig. 5(a)]; 2) a Landsat-7 ETM+ subimage of a seaside area in Sicily, Italy, 400 \times 400 pixels in size, path: 188, row: 034, acquisition date: September 26, 1999 (see Fig. 9); and 3) a Landsat-7 ETM+ subimage of a mountainous snow-covered area in Northern Italy, 400 \times 400 pixels in size, path: 193, row: 028, acquisition date: September 13, 1999 (see Fig. 10).

These three radiometrically calibrated seven-band Landsat-7 ETM+ subimages are suitable for comparing the novel fuzzy LSRC against the original crisp LSRC proposed in [14] (refer to Section III).

To test the fuzzy SSRC, AVSRC, and ISRC subsystems against their crisp counterparts (refer to Section V-A) [15], synthetic sensor-specific radiometrically calibrated MS images are generated from the three test seven-band Landsat subimages shown in Figs. 5(a), 9, and 10. The synthetic subimages are generated as follows.

- 1) SSRC requires as input a four-band (G, R, near-IR (NIR), MIR1) SPOT-like imagery. Thus, the Landsat bands B, MIR2, and TIR are removed from the three test Landsat subimages (see Table II).
- 2) AVSRC requires as input a four-band (R, NIR, MIR1, TIR) AVHRR-like imagery. Thus, the Landsat bands B,

G, and MIR2 are removed from the three test Landsat subimages (see Table II).

- 3) ISRC requires as input a four-band (B, G, R, NIR) IKONOS-like imagery. Thus, the Landsat bands MIR1, MIR2, and TIR are removed from the three test Landsat subimages (see Table II).

The proposed MS image selection/generation strategy allows sensitivity analysis of the fuzzy LSRC, SSRC, AVSRC, and ISRC systems [16], [19]. Differences in performance among these classifiers are exclusively due to differences in spectral resolution of the given set of test images (sharing the same geographic footprint, time of acquisition, sensor calibration, and SR).

It is noteworthy that, according to some reviewers, “the generation of these “synthetic” images appears to be critical. Synthetic bands are selected on the basis of their wavelength range exclusively, while optical sensor parameters such as SR, spectral response functions, swath width, incident angle, etc., are ignored. Thus, the use of synthetic images seems interesting in regard to missing spectral information, but not in regard to the transferability of the approach to other sensor sources.” This skepticism is reasonable, but not justified. It is obvious to say that synthetic and real-world images are complementary and by no means alternative for testing [62], [63]. For example, say that SRC is capable of detecting spectral signatures typical of red apples, yellow bananas, and orange oranges. At a given SR, let a picture of apples and bananas be taken. If a pixel is a mixture of red apples and yellow bananas, then that pixel looks orange. Since SRC is assumed to be provided with an orange object model, it labels that mixed pixel as orange like an orange. This pixel mapping (for example, that pixel looks like an orange) is strictly correct, although SRC fails to provide any information about pixel unmixing. If the same picture of apples and bananas is taken at a finer SR capable of reducing the presence of mixed pixels to null, then the SRC orange detector would never fire and all image pixels would be labeled by SRC as either red (like an apple) or yellow (like a banana). To conclude, if the spatial/spectral resolution of an MS image varies, then the behavior of the SRC must vary, but remain consistent with the varying image information content.

C. Fuzzy SRC System Consistency Checks and Model Selection Criteria

1) *Consistency Checks*: The following consistency checks are scheduled to verify the adequacy of the fuzzy SRC version against both theory and the reference crisp SRC implementation.

- 1) Relationship $(\text{MPM EQ True}) \supseteq (MWC > 1)$ holds $\forall \alpha \geq 0$. As a special case, if $\alpha = 0$, then equality $(\text{MPM EQ True}) == (MWC > 1)$ must hold (refer to Section IV-E).
- 2) If the fuzzy S- and Z-function bandwidth parameter $0 < \Delta b = b - a = c - b$ tends to zero, i.e., if $\Delta b \rightarrow 0$, then $a \rightarrow b = Th \rightarrow c$. In practice, if $\Delta b \rightarrow 0$, then the fuzzy SRC adopts crisp S- and Z-functions (see Section II-A). If $\Delta b \rightarrow 0$, the fuzzy SRC consistency checks can be twofold.

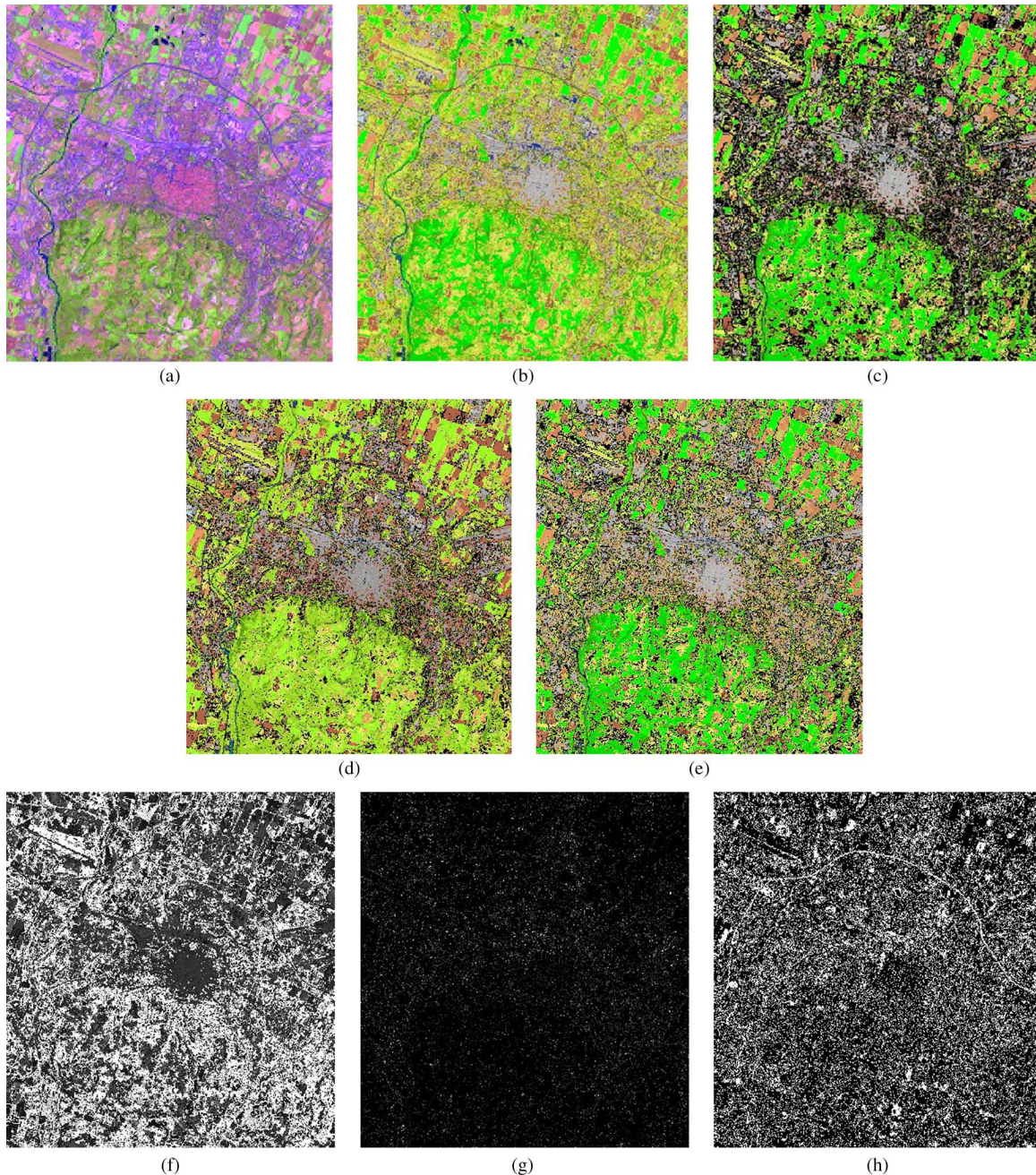


Fig. 5. (a) Zoomed image of the city of Bologna, Italy, extracted from a Landsat 7 ETM+ image (path: 192, row: 029, acquisition date: June 20, 2000), radiometrically calibrated into TOARF values and depicted in false colors (R: band TM5 = MIR1, G: band TM4 = NIR, B: band TM1 = B). (b) Preliminary classification map, depicted in pseudocolors, automatically generated by the crisp LSRC from the radiometrically calibrated image shown in (a). Map legend is shown in Fig. 2. The association of symbolic spectral categories with pseudocolors found in nature allows an intuitive (qualitative, visual) assessment of the preliminary classification map accuracy in comparison with the input image depicted in false colors, as shown in (a). (c) Preliminary classification map, depicted in pseudocolors, generated by the fuzzy LSRC from the radiometrically calibrated image shown in (a), with bandwidth $\Delta b = 0$. Map legend is shown in Fig. 2. Multiple winners, i.e., pixels featuring ($MWC > 1$), are depicted in black. They are due to the fact that the hierarchical structure of the crisp (L)SRC has been replaced by a flat modular organization of the fuzzy SRC. In line with theory, the fuzzy LSRC with $\Delta b = 0$ looks the same as (b) aside from the multiple winners depicted in black. (d) Preliminary classification map, depicted in pseudocolors, generated by the fuzzy LSRC from the radiometrically calibrated image shown in (a), with $b = Th$ and bandwidth $\Delta b = b - a = c - b = 5$. Map legend is shown in Fig. 2. Multiple winners, i.e., pixels featuring ($MWC > 1$), are depicted in black. In (d), the occurrence of black labels is inferior to that in (c), but pseudocolors appear shifted from those visible in (b), although no major semantic shift occurs. For example, comparing (b) with (d) reveals an intensity reduction of green pseudocolors in the latter. This corresponds to a reduction of the LAI associated with spectral categories belonging to the same spectral supercategory "vegetation." (e) Preliminary classification map, depicted in pseudocolors, generated by the fuzzy LSRC from the radiometrically calibrated image shown in (a), with $b = Th$ and full bandwidth $\Delta B = c - a = 0.10 \times Th$. Map legend is shown in Fig. 2. Multiple winners, i.e., pixels featuring ($MWC > 1$), are depicted in black. The occurrence of black labels is inferior to (better than) that in (d), and pseudocolors are the same as those visible in (b). (f) Continuous MMB image, with MMB values in range $[0, 1]$ transformed into $\{0, 255\}$. MMB values are depicted in gray tones ranging from black, corresponding to ($MMB == 0$), to white, corresponding to ($MMB == 255$). (g) Discrete MWC image, with MWC values ≥ 1 . Multiple winners, i.e., pixels featuring ($MWC > 1$), are depicted in gray tones; otherwise, if ($MWC == 1$), pixels are depicted in black. For curiosity, in this image, $\max(MWC) = 5$. (h) Binary MPM map with $\alpha = 0.2$, where mixed pixels include multiple winners, i.e., (MPM EQ True) \supseteq ($MWC > 1$) $\forall \alpha \geq 0$. If (MPM EQ True), then pixels are depicted in white; otherwise, they are black. It is interesting to note that, in line with theoretical expectations, mixed pixels largely correspond to boundary pixels, i.e., pixels lying across (2-D) object boundaries.

- a) In the special case of $\Delta b \rightarrow 0$, it must hold true that the classification maps generated by the crisp SRC and the fuzzy SRC look the same (see Section I) aside from multiple winners identified by the fuzzy SRC, where ($MWC > 1$) (refer to Section IV-F). To replicate the crisp SRC output map with the fuzzy SRC where $\Delta b \rightarrow 0$, then multiple winners must be defuzzified (hardened) in line with the order of presentation of the sorted set of spectral categories adopted by the crisp SRC [14]–[17].
- b) The fuzzy MMB output image must become equal to 255 image-wide, except where pixels are assigned to spectral category “outliers,” corresponding to the conventional MMB value equal to zero (refer to Section IV-E).

2) *Fuzzy SRC System QIs*: The purpose of SRC fuzzification is to keep the novel fuzzy SRC consistent with its benchmark, the crisp SRC, unless mixed pixels are detected by the former (refer to Section IV-E), which is its added value (see Section I). To achieve this objective, the following fuzzy SRC system QIs should be optimized simultaneously.

- 1) To maximize interspectral category separability, the number of multiple winners, where ($MWC > 1$) (refer to Section IV-E), should be minimized image-wide. By paradoxical reasoning, if the number of multiple winners is maximized, i.e., becomes equal to image size, which means that every pixel is a “multiple winner,” then the discrimination capability of the classifier reduces to zero.
- 2) To maximize interspectral category separability, the number of mixed pixels, where (MPM EQ True) (refer to Section IV-E), should be minimized image-wide, refer to point 1). It is noteworthy that the goal of minimizing the number of mixed pixels is less relevant than the minimization of multiple winners representing the “worst case,” such that ($MWC > 1$) \subseteq (MPM EQ True) (refer to Section IV-F).
- 3) Semantic differences between the crisp (master) and the fuzzy (slave) SRC map should be minimized in terms of the following.
 - a) Major semantic differences, also called semantic shifts. For example, if the same pixel is labeled as “vegetation” in one preliminary classification map and, for example, “either bare soil or built-up” in the other map (refer to Section III), this semantic difference is relevant and must be straightened out, i.e., either one of the two classification maps is wrong or both are wrong.
 - b) Minor semantic differences, i.e., changes in subcategories belonging to the same spectral supercategory (refer to Section III). For example, if the same pixel is labeled as “strong vegetation” in one preliminary classification map and labeled as “average vegetation” in the other map [14], there is no semantic shift, but a minor semantic difference to be straightened out, i.e., either one of the two classification maps is wrong or both are wrong.

It is noteworthy that the introduction of semantic-based QIs, such as those proposed in the aforementioned points 3a) and 3b), in combination with traditional metrological/statistically

based QIs, related to subsymbolic continuous variables, such as QIs in points 1) and 2), is one of the advantages introduced by the proposed two-stage stratified hierarchical hybrid RS-IUS architecture comprising a pixel-based preliminary classification first stage [13]–[19].

D. Selection of the Reference Data Set

The following four spectral categories [where spectral category means LC class set (refer to Section III and [15]–[17])] are selected: 1) “either woody vegetation or cropland or grassland,” identified as “vegetation” (V); 2) (shrub and brush) “rangeland” (R); 3) “either bare soil or built-up” (BB); and 4) “water” (W). According to Section II-D, the required cardinality of reference samples per target spectral category is set equal to $m_{\text{test},c} = 350$, $c = 1, \dots, C$, where $C = 4$.

To begin with, reference samples are selected for the test image shown in Fig. 5(a) (refer to Section VI-A1b). They consist of “pure” pixels manually selected in the test image by the author, who acts as domain expert. In other words, in the selection of the reference data set, boundary pixels in transitional areas are avoided, which is a typical choice in machine learning applications to RS data classification. These reference samples are validated on a VHR spaceborne image provided by a commercial 3-D Earth viewer [e.g., Google Earth (see Fig. 11)].

It is noteworthy that, in Fig. 5(a), only 50 pure pixels belonging to class W are identified manually image-wide. Thus, for class W, if (4) is applied where $m_c = 50$ and $p_{\text{OA},c} = 85\%$, then $\delta_c = 13\%$.

Since $M_{\text{test}} = 350 \times 3 + 50 = 1100$ and the target overall classification accuracy probability $p_{\text{OA}} = 85\%$ at a confidence level = 95%, then the half width δ of the error tolerance $\pm\delta$ becomes $\delta = (1) = \text{sqrt}(((1.96)^2 \times 0.85 \times 0.15)/1100) = 2\%$.

VI. DISCUSSION OF EXPERIMENTAL RESULTS

The four fuzzy LSRC, SSRC, AVSRC, and ISRC subsystems of the integrated fuzzy SRC system of systems (refer to Section III) are quantitatively compared against their crisp counterparts (refer to Section V-A) in three classification experiments. In these experiments, the test data set consists of the Landsat image shown in Fig. 5(a), 9, and 10, respectively (refer to Section V-B).

A. Crisp to Fuzzy LSRC Transformation

1) *First Test Image: City Area of Bologna, Italy*: The fuzzy LSRC is compared against the crisp LSRC when the seven-band Landsat image shown in Fig. 5(a) is employed as input. Generated from Fig. 5(a), the crisp LSRC map, shown in Fig. 5(b), represents the reference (master) map.

a) *Optimization of the bandwidth parameter Δb by the domain expert based on evidence from data:*

- 1) $\Delta b \rightarrow 0$

The first consistency check proposed in Section V-C1 is tested when the bandwidth parameter $\Delta b \rightarrow 0$ and the input image is that shown in Fig. 5(a). In line with

expectations, the fuzzy LSRC map, shown in Fig. 5(c), coincides with Fig. 5(b) aside from multiple winners, i.e., pixels where $(MWC > 1)$, depicted in black in Fig. 5(c).

2) Nonadaptive $\Delta b > 0$

When a nonzero bandwidth parameter $\Delta b > 0$ is fixed image-wide, e.g., $\Delta b = 5$, such that parameters $b = Th$, $a = Th - 5$, and $c = Th + 5$ in (1) and (2), then the fuzzy LSRC (slave) map becomes the one shown in Fig. 5(d). In Fig. 5(d), the occurrence of multiple winners, depicted in black, featuring $(MWC > 1)$, decreases [improves (refer to Section V-C2)] with respect to that in Fig. 5(c). However, the comparison of Fig. 5(d) with Fig. 5(b) reveals an undesirable reduction of intensity of green pseudocolors in the slave map with respect to the master map. This corresponds to minor semantic shifts among subcategories belonging to spectral supercategory “vegetation” (see Section III). Fortunately, no major semantic shift (refer to Section V-C2) appears to occur in Fig. 5(d) with respect to Fig. 5(b).

3) Adaptive $\Delta b = f(Th) > 0$

In place of a bandwidth parameter Δb fixed image-wide, a bandwidth Δb value adaptive to the crisp threshold value $b = Th$ is tested. The simplest kind of adaptive bandwidth Δb value is computed as a fixed percentage P (% , with $P > 0$) of the crisp Th value. Percentage P values ranging from 10% to 150% of the Th value, in 10% steps, are tested for the so-called *full bandwidth* parameter ΔB . This is defined as $\Delta B = 2 \times \Delta b = c - b + b - a = c - a$, with $a < b = Th < c$, such that $\Delta B > 0$. Therefore, by definition, if $\Delta B = P \times Th$, then $a = [(1 - 0.5 \times P) \times Th]$ and $c = [(1 + 0.5 \times P) \times Th]$.

In Fig. 5(e), where $\Delta B = 0.10 \times Th$, the occurrence of multiple winners, where $(MWC > 1)$, is inferior to (better than) the number of multiple winners in Fig. 5(d). In addition, no semantic shift occurs in comparison with Fig. 5(b).

When $\Delta B = 1.30 \times Th$, the occurrence of pixels featuring $(MWC > 1)$ is inferior to (better than) that in Fig. 5(e) and no semantic shift occurs in comparison with Fig. 5(b). In practice, this fuzzy LSRC output map appears almost indistinguishable from Fig. 5(b); thus, it is not shown in this paper.

The conclusion of the aforementioned experiments 1)–3) is that the choice $\Delta B = 1.30 \times Th$ is preferred to $\Delta B = 0.10 \times Th$. In the case of $\Delta B = 1.30 \times Th$, the three fuzzy SRC-specific output products, namely, MMB, MWC, and MPM (refer to Section IV-E), are those shown in Figs. 5(f)–(h). In line with theory, Figs. 5(g) and (h) satisfy the constraint $(MPM \text{ EQ True}) \supseteq (MWC > 1)$, with $\alpha = 0.2$ (refer to Section V-C1). In addition, it is interesting to note that, in line with theoretical expectations, mixed pixels where $(MPM \text{ EQ True})$, shown in Fig. 5(h), largely correspond to boundary pixels, i.e., pixels lying across (2-D) object boundaries.

According to Section V-C2, multiple winners should be minimized with the highest priority while mixed pixels should be minimized with lower priority. Fig. 6 shows curves of the image-wide numbers of multiple winners, where $(MWC > 1)$, and mixed pixels, where $(MPM \text{ EQ True}) \supseteq (MWC > 1)$, $\forall \alpha \geq 0$ (refer to Section IV-F), as functions of the

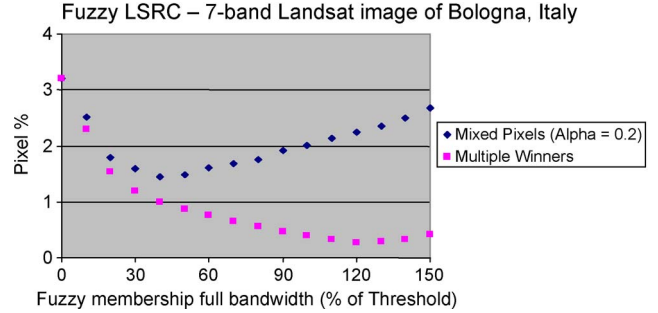


Fig. 6. Fuzzy LSRC. Multiple winners, where $(MWC > 1)$, and mixed pixels, where $(MPM \text{ EQ True})$, versus fuzzy membership full bandwidth values, where $\Delta B = c - a = P \times Th$, with P ranging from 0% to 150% with 10% steps while Th is fixed according to [14, Tab. III]. Input seven-band Landsat image shown in Fig. 5(a). The number of multiple winners is minimized when $\Delta B = 1.3 \times Th$ while the number of mixed pixels is minimized when $\Delta B = 0.4 \times Th$.

TABLE III
CONFUSION MATRIX OF BOTH THE CRISP SRC AND THE “HARDENED” FUZZY SRC WHEN THE TEST IMAGE IS THAT SHOWN IN FIG. 5(a)

		Ground Truth (Pixels)			
		V	R	BB	W
Predicted class	V	350			
	R		350		
	BB			350	
	W				50
		Sum of diagonals = 1100. Sum of entries = 110.			
		p_{OA} = Overall Accuracy = $1100 / 1100 = 1.00 \pm 2\%$.			

varying percentage P ranging from 10% to 150% in 10% steps, such that $\Delta B = P \times Th$ (see earlier discussion). In line with Section V-C1, Fig. 6 shows that relationship $(MPM \text{ EQ True}) \supseteq (MWC > 1)$, with $\alpha = 0.2$, holds true $\forall P \in \{0, 0.1, \dots, 1.5\}$. Fig. 6 also shows that the number of pixels featuring $(MWC > 1)$ is minimized when $\Delta B = 1.30 \times Th$ while the number of pixels featuring $(MPM \text{ EQ True})$ is minimized when $\Delta B = 0.40 \times Th$. According to Section V-C2, the former minimization criterion overcomes the latter. To conclude, $\Delta B = 1.30 \times Th$ is the favorite choice in this first experiment where the fuzzy LSRC is input with the seven-band Landsat image shown in Fig. 5(a).

b) *Classification accuracy*: Table III shows the confusion matrix holding for both the crisp and the fuzzy LSRC with respect to the four-class reference data set selected in Section V-D. The OA probability estimate $p_{OA} = 100\% \pm 2\%$ is neither surprising nor very significant. It means that, in line with theoretical expectations and results found in previous papers [13]–[19], the crisp and fuzzy LSRCs are both accurate in the recognition of spectral signatures of pure pixels belonging to different spectral categories (not to be confused with traditional LC classes [15]–[17]). Similar considerations hold for the crisp and fuzzy SRCs applied across the selected test images and sensors [LSRC, SSRC, AVSRC, and ISRC (refer to Section V-A)]. Therefore, these additional sample error matrices are not reported in the rest of this paper.

To investigate image-wide differences between the crisp and fuzzy LSRCs, Table IV shows the error matrix of the hardened fuzzy LSRC map [where multiple winners are defuzzified (refer

TABLE IV
 CONFUSION MATRIX OF THE “HARDENED” FUZZY SRC MAP WITH RESPECT TO THE CRISP SRC MAP EMPLOYED AS THE GROUND TRUTH WHEN THE TEST IMAGE IS THAT SHOWN IN FIG. 5(a). THE MOST RELEVANT SEMANTIC TRANSITIONS ARE HIGHLIGHTED IN LIGHT AND DARK GRAY

		Ground Truth (Pixels), crisp SRC							
		V	R	WR	BB	WASH	CL	TNCL	SN
Predicted spectral categories, “hardened” fuzzy SRC	V	67362				27			
	R		37990	185	6				
	WR			15479					
	BB		2118	8567	41229	23			
	WASH					614			
	CL								
	TNCL								
	SN								
Total in pixels		67362	40108	24231	41235	664	0	0	0
Sum of diagonals = 162674. Sum of entries = 173600. ρ_{OA} = Overall Accuracy = 162674/173600 = 0.937 ± 0%.									

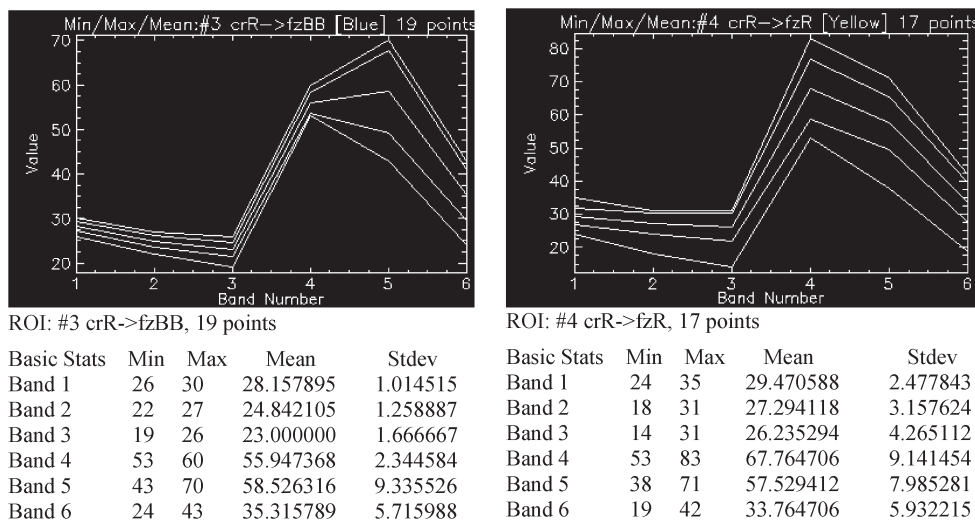


Fig. 7. Two regions of interest. Min, max, mean, and mean ± Stdev curves are depicted (taken from ENVI). x-axis: Spectral band index (TM1 = 1, . . . , TM5 = 5, TM7 = 6). Y-axis: TOARF values in [0, 1] rescaled into {0, 255}.

to Section V-C1]] in comparison with the crisp LSRC map employed as ground truth. In this image-wide error matrix, the spectral categories are as follows: 1) “either woody vegetation or cropland or grassland,” identified as “vegetation” (V); 2) (shrub and brush) “rangeland” (R); 3) “weak rangeland” (WR); 4) “either bare soil or built-up” (BB); 5) “either water or shadow” (WASH); 6) “clouds” (CL); 7) “thin clouds” (TNCL); and 8) “either snow or ice” (SN) [14]. According to Section V-C2, semantic differences between the crisp and hardened fuzzy SRC map should be as few as possible.

Table IV reveals that, in this experiment, the most frequent semantic transitions occur between crisp R into the hardened fuzzy BB, identified as (crR ⇒ fzBB), and crisp WR into the hardened fuzzy BB, identified as (crWR ⇒ fzBB). The first case, where (crR ⇒ fzBB), is examined as follows: Two sets of isolated pixels scattered throughout the test image are selected such that (crR ⇒ fzBB) in the first set and (crR ⇒ fzR) in the second set. It is found that all these reference pixels belong to the set of multiple winners, which means that these pixels are among those difficult to label. Spectral signatures in TOARF values of the two sets (crR ⇒ fzBB) and (crR ⇒ fzR) are shown in Fig. 7. The spectral signature of (crR ⇒ fzR) on the right of Fig. 7 shows two spectral properties typical of vegetation, namely: 1) the (Band 4/Band 3) ratio (proportional to

canopy chlorophyll absorption [15], [40]) is superior to that in the left case (crR ⇒ fzBB) and 2) Band 5 reflects (slightly) less than Band 4 (due to canopy water absorption [32], [40]). The conclusion is that the fuzzy SRC is correct in the discrimination between the two sets of pixels (crR ⇒ fzBB) and (crR ⇒ fzR) considered indistinguishable by the crisp SRC.

The same procedure is adopted to investigate semantic transitions occurring between crisp WR into the hardened fuzzy BB, i.e., (crWR ⇒ fzBB). Two sets of isolated pixels scattered throughout the test image are selected such that (crWR ⇒ fzBB) in the first set and (crWR ⇒ fzWR) in the second set. Their spectral signatures in TOARF values are shown in Fig. 8. According to observations similar to those found in the previous paragraph, the comparison of these two spectral signatures reveals that the fuzzy SRC is correct in the discrimination between the two sets of pixels (crWR ⇒ fzBB) and (crWR ⇒ fzWR) considered indistinguishable by the crisp SRC.

It is noteworthy that the main difference between the spectral signatures of spectral category fzR, shown in Fig. 7 on the right, and the spectral signatures of spectral category fzWR, shown in Fig. 8 on the right, is that the former features a slightly superior (Band 4/Band 3) ratio (proportional to canopy chlorophyll absorption [15], [40]). This is additional evidence of the high accuracy and sensitivity of the fuzzy SRC.

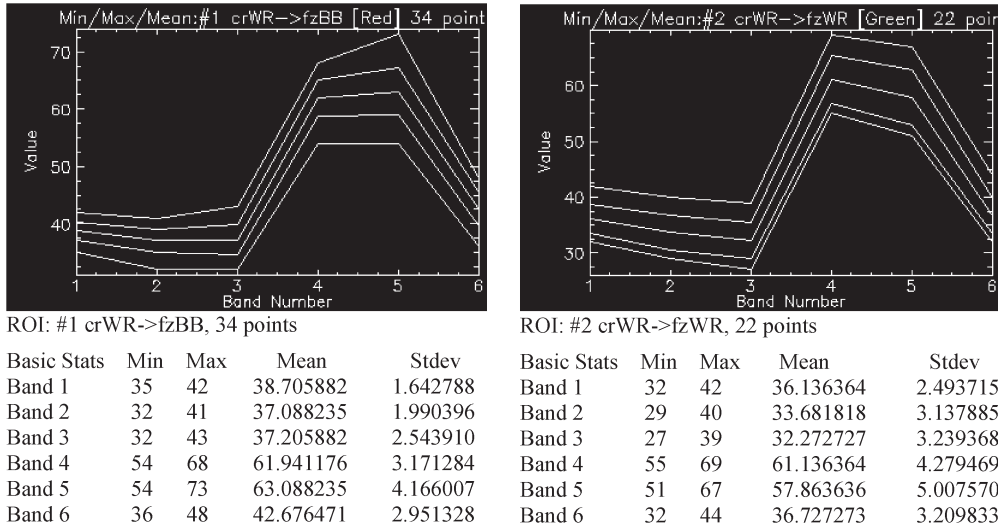


Fig. 8. Two regions of interest. Min, max, mean, and mean \pm Stdev curves are depicted (taken from ENVI). x-axis: Spectral band index (TM1 = 1, . . . , TM5 = 5, TM7 = 6). Y-axis: TOARF values in [0, 1] rescaled into {0, 255}.

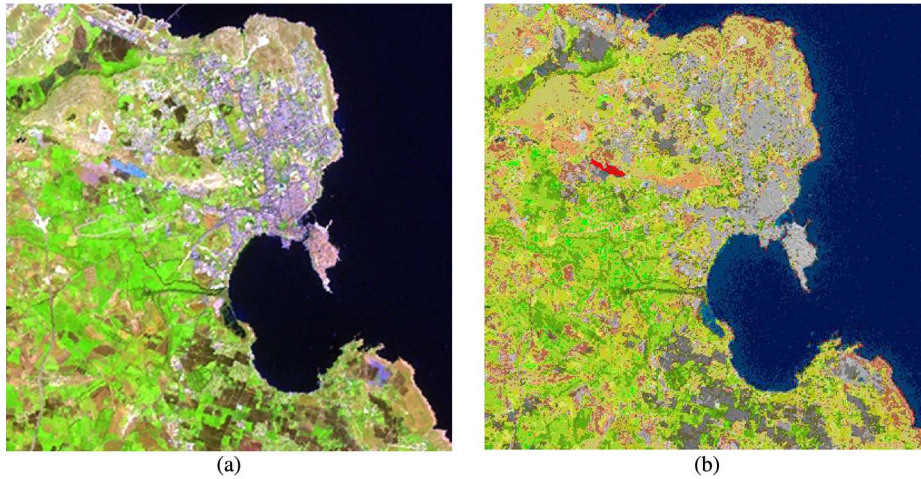


Fig. 9. (a) Zoomed image of Sicily, Italy, extracted from a Landsat 7 ETM+ image (path: 188, row: 034, acquisition date: September 26, 1999), radiometrically calibrated into TOARF values and depicted in false colors (R: band TM5 = MIR1, G: band TM4 = NIR, B: band TM1 = B). (b) Preliminary classification map, depicted in pseudocolors, automatically generated by the crisp LSRC from the radiometrically calibrated image shown in (a). Map legend shown in Fig. 2.

2) Second Test Image: Coastal Area of Sicily, Italy:

a) Optimization of the bandwidth parameter Δb by the domain expert based on evidence from data: The reference crisp LSRC classification map, automatically generated from the second test Landsat subimage of Sicily, shown in Fig. 9(a), is shown in Fig. 9(b).

The same type of graph shown in Fig. 6 is generated when the fuzzy LSRC is input with the second test Landsat subimage shown in Fig. 9. In this new graph (omitted to reduce paper length), relationship (MPM EQ True) \supseteq ($MWC > 1$), with $\alpha = 0.2$, holds $\forall P \in \{0, 0.1, \dots, 1.5\}$, in line with theoretical expectations (see Section V-C1). In addition, this graph shows a minimum in the number of multiple winners, where ($MWC > 1$), when $\Delta B = 1.30 \times Th$ while the number of mixed pixels, where (MPM EQ True), is minimized when $\Delta B = 0.40 \times Th$.

To conclude, $\Delta B = 1.30 \times Th$ is the favorite choice in this second experiment where the fuzzy LSRC is input with the seven-band Landsat image shown in Fig. 9(a).

b) Classification accuracy: Table V reveals that, in this experiment, the most relevant semantic transitions occur between crisp R into the hardened fuzzy BB (crR \Rightarrow fzBB) and crisp WR into the hardened fuzzy BB (crWR \Rightarrow fzBB). The same conclusions reported in Section VI-A1b hold here in favor of the fuzzy SRC discrimination capability.

3) Third Test Image: Mountainous Area in Northern Italy:

a) Optimization of the bandwidth parameter Δb by the domain expert based on evidence from data: The reference crisp LSRC classification map, shown in Fig. 10(b), is automatically generated from the third test Landsat subimage of Northern Italy shown in Fig. 10(a). Next, this third test subimage is input to the fuzzy LSRC to generate as output the same type of graph shown in Fig. 6. In this new graph (omitted to reduce paper length), relationship (MPM EQ True) \supseteq ($MWC > 1$), with $\alpha = 0.2$, holds $\forall P \in \{0, 0.1, \dots, 1.5\}$, in line with theoretical expectations (see Section V-C1). In addition, this graph shows a minimum in the number of pixels featuring ($MWC > 1$)

TABLE V
CONFUSION MATRIX OF THE HARDENED FUZZY SRC MAP WITH RESPECT TO THE CRISP SRC MAP EMPLOYED AS THE GROUND TRUTH WHEN THE TEST IMAGE IS THAT SHOWN IN FIG. 9. THE MOST RELEVANT SEMANTIC TRANSITIONS ARE HIGHLIGHTED IN LIGHT AND DARK GRAY

		Ground Truth (Pixels), crisp SRC							
		V	R	WR	BB	WASH	CL	TNCL	SN
Predicted spectral categories, "hardened" fuzzy SRC	V	27524				15			
	R		18435	179	8				
	WR			16331	726				
	BB		1824	10209	35439	29			
	WASH					49281			
	CL								
	TNCL								
	SN								
Total in pixels		27524	20259	26719	36173	49325	0	0	0
Sum of diagonals = 147010. Sum of entries = 160000. $POA = \text{Overall Accuracy} = 147010/160000 = 0.919 \pm 0\%$.									

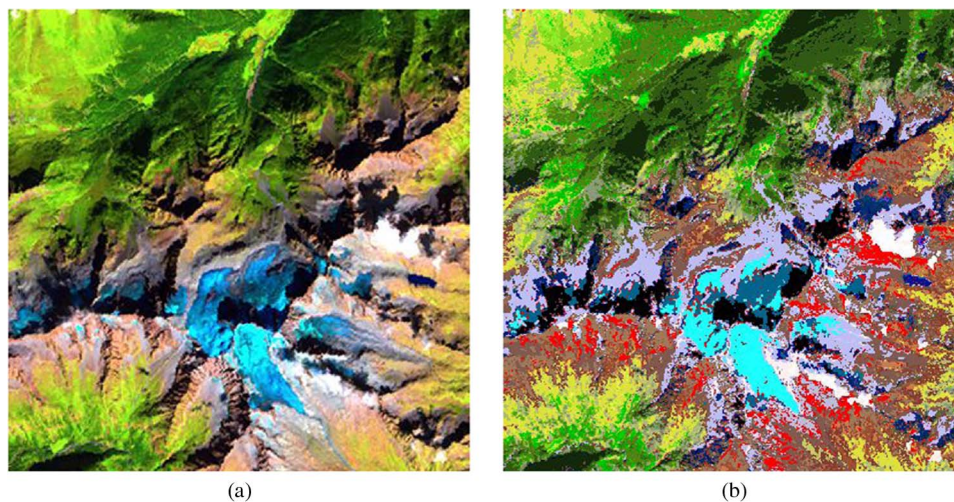


Fig. 10. (a) Zoomed image of Northern Italy, extracted from a Landsat 7 ETM+ image (path: 193, row: 028, acquisition date: September 13, 1999), radiometrically calibrated into TOARF values, and depicted in false colors (R: band TM5 = MIR1, G: band TM4 = NIR, B: band TM1 = B). (b) Preliminary classification map, depicted in pseudocolors, automatically generated by the crisp LSRC from the radiometrically calibrated image shown in (a). Map legend shown in Fig. 2.

when $\Delta B = 1.20 \times Th$, while the number of pixels featuring (MPM EQ True) is minimized when $\Delta B = 0.40 \times Th$.

To conclude, $\Delta B = 1.20 \times Th$ is the favorite choice in this third experiment where the fuzzy LSRC is input with the seven-band Landsat image shown in Fig. 10(a).

b) Classification accuracy: Table VI reveals, that in this experiment, the most relevant semantic transitions occur between crisp R into the hardened fuzzy BB ($crR \Rightarrow fzBB$), crisp WR into the hardened fuzzy BB ($crWR \Rightarrow fzBB$), and crisp TNCL into the hardened fuzzy BB ($crTNCL \Rightarrow fzBB$). For the first two semantic transitions, the same conclusions reported in Section VI-A1b hold. About the third transition ($crTNCL \Rightarrow fzBB$), it is not surprising because, per se, spectral category TNCL is rather called "either thin clouds over water or dark-toned bare soils in mountainous areas." By visual interpretation of the target image shown in Fig. 10, pixels labeled as $crTNCL$ appear to belong to a dark-toned bare soil whose detection is made more explicit by the fuzzy SRC through label $fzBB$. This conclusion is in favor of the fuzzy SRC discrimination capability.

These fuzzy LSRC accuracy results hold for the downscaled LSRC subsystems being tested, namely, SSRC, AVSRC, and

ISRC. Therefore, no additional classification accuracy is reported in the rest of this paper.

4) Computation Time: In terms of computation time, the crisp and fuzzy LSRC algorithms implemented in the C++ programming language require 5'50" and 7'50", respectively, to generate the map shown in Fig. 11 from a full Landsat-7 ETM+ scene (path: 192, row: 029, acquisition date: June 20, 2000, 8065 × 7000 pixels in size) in a single-process single-thread run on a standard desktop computer provided with a Dual Core Pentium processor. Thus, the fuzzy LSRC version takes 31% more time to run than the crisp LSRC version.

B. Crisp to Fuzzy SSRC Transformation

The fuzzy SSRC S- and Z-MFs' full bandwidth parameter $\Delta B = P \times Th$ (refer to Section VI-A1a) is optimized across the four-band SPOT-like images synthesized from the seven-band Landsat subimages shown in Figs. 5(a), 9, and 10 (refer to Section V-B). Three graphs, similar to that shown in Fig. 6, are generated from these three fuzzy SSRC experiments. In these three graphs (omitted to reduce paper length), the number of multiple winners is minimized when $\Delta B = 1, 50 \times Th$ for

TABLE VI
 CONFUSION MATRIX OF THE HARDENED FUZZY SRC MAP WITH RESPECT TO THE CRISP SRC MAP EMPLOYED AS THE GROUND TRUTH WHEN THE TEST IMAGE IS THAT SHOWN IN FIG. 11. THE MOST RELEVANT SEMANTIC TRANSITIONS ARE HIGHLIGHTED IN LIGHT AND DARK GRAY

		Ground Truth (Pixels), crisp SRC							
		V	R	WR	BB	WASH	CL	TNCL	SN
Predicted spectral categories, "hardened" fuzzy SRC	V	51289				207			2
	R	8	22304	53	17				31
	WR			2591	97				10
	BB		1295	1451	53421	85	385	2600	
	WASH					4216			
	CL						1693		
	TNCL						875	10506	
SN								76	6788
Total in pixels		51297	23599	4095	53535	4508	2953	13225	6788
Sum of diagonals = 152808. Sum of entries = 160000. p_{OA} = Overall Accuracy = 152808/160000 = 0.955 ± 0%.									

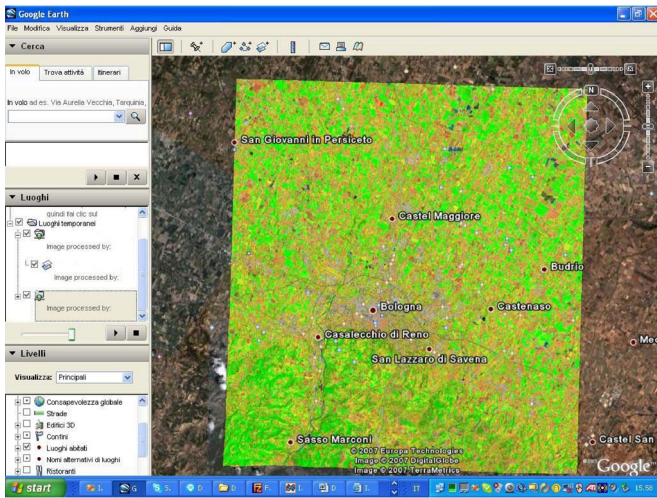


Fig. 11. Preliminary spectral map, depicted in pseudocolors, generated by LSRC from a Landsat 7 ETM+ image of the city area of Bologna, Italy (acquisition date: June 20, 2000, SR: 30 m, path = 192, row = 029), radiometrically calibrated into TOA reflectance. The test image shown in Fig. 5(a) is extracted from this Landsat image. The LSRC map is transformed into the kml data format and loaded as a thematic layer in a commercial 3-D earth viewer (e.g., Google Earth).

all test images. As a secondary consideration, the number of mixed pixels is minimized at $\Delta B = 0.80 \times Th$ [first synthetic test image generated from Fig. 5(a)], $\Delta B = 0.60 \times Th$ (second synthetic test image generated from Fig. 9), and $\Delta B = 0.90 \times Th$ (third synthetic test image generated from Fig. 10), respectively.

To summarize, $\Delta B = 1.50 \times Th$ is the favorite choice in the three experiments where the fuzzy SSRC is tested.

C. Crisp to Fuzzy AVSRC Transformation

The fuzzy AVSRC S- and Z-MFs' full bandwidth parameter $\Delta B = P \times Th$ (refer to Section VI-A1a) is optimized across the four-band AVHRR-like images synthesized from the seven-band Landsat subimages shown in Figs. 5(a), 9, and 10 (refer to Section V-B). Three graphs, similar to that shown in Fig. 6, are generated from these three fuzzy AVSRC experiments. In these three graphs (omitted to reduce paper length), the number of multiple winners is minimized at $\Delta B = 1.30 \times Th$ [first synthetic test image generated from Fig. 5(a)], $\Delta B = 1.40 \times Th$ (second synthetic test image generated from Fig. 9),

and $\Delta B = 0.80 \times Th$ (third synthetic test image generated from Fig. 10), respectively. As a secondary consideration, the number of mixed pixels is minimized at $\Delta B = 0.40 \times Th$ [first synthetic test image generated from Fig. 5(a)], $\Delta B = 0.70 \times Th$ (second synthetic test image generated from Fig. 9), and $\Delta B = 0.40 \times Th$ (third synthetic test image generated from Fig. 10), respectively.

To summarize, there is no unique best value of P , such that $\Delta B = P \times Th$, across the three experiments where the fuzzy AVSRC is tested.

D. Crisp to Fuzzy ISRC Transformation

The fuzzy ISRC S- and Z-MFs' full bandwidth parameter $\Delta B = P \times Th$ is optimized across the four-band IKONOS-like images synthesized from the seven-band Landsat subimages shown in Figs. 5(a), 9, and 10 (refer to Section V-B). Three graphs, similar to that shown in Fig. 6, are generated from these three fuzzy ISRC experiments. In these three graphs (omitted to reduce paper length), the number of multiple winners is minimized at $\Delta B = 1.00 \times Th$ [first synthetic test image generated from Fig. 5(a)], $\Delta B = 1.10 \times Th$ (second synthetic test image generated from Fig. 9), and $\Delta B = 1.50 \times Th$ (third synthetic test image generated from Fig. 10), respectively. As a secondary consideration, the number of mixed pixels is minimized at $\Delta B = 0.40 \times Th$ [first synthetic test image generated from Fig. 5(a)], $\Delta B = 0.00 \times Th$ (second synthetic test image generated from Fig. 9), and $\Delta B = 0.50 \times Th$ (third synthetic test image generated from Fig. 10), respectively.

To summarize, there is no unique best value of P , such that $\Delta B = P \times Th$, across the three experiments where the fuzzy ISRC is tested.

E. Comments

To minimize the number of multiple winners or the number of mixed pixels according to the fuzzy SRC quality criteria proposed in Section V-C2, the fuzzy S- and Z-MFs' full bandwidth parameter $\Delta B = P \times Th$ clearly depends on the MS image and optical imaging sensor at hand. However, if we accept that the percentage of multiple winners and mixed pixels can range up to 20% above their minima, then the domain of change of the fixed percentage P of the crisp threshold value Th across images and sensors becomes $P \in [1.10, 1.40]$ to minimize

TABLE VII
TOLERANCE INTERVAL ACROSS IMAGES AND SENSORS OF THE PERCENTAGE PARAMETER P , SUCH THAT $\Delta B = P \times TH$, BECOMES $P \in [1.10, 1.40]$ TO MINIMIZE THE NUMBER OF MULTIPLE WINNERS UP TO 20% ABOVE THE MINIMUM AND $P \in [0.4, 0.5]$ TO MINIMIZE THE NUMBER OF MIXED PIXELS UP TO 20% ABOVE THE MINIMUM

Fuzzy SRC system of systems	Test case	Test data set	'Mixed pixel' occurrence (up to 20% above the minimum): P values	'Multiple winner' occurrence (up to 20% above the minimum): P values
7-band Fuzzy LSRC	1	Urban area of Bologna, Italy, in the 7-band Landsat	[0.30, 0.70]	[1.10, 1.40]
	2	Coastal area of Sicily in the 7-band Landsat	[0.10, 0.50]	[1.10, 1.40]
	3	Mountainous area in Northern Italy in the 7-band Landsat	[0.20, 0.50]	[1.00, 1.40]
4-band Fuzzy SSRC	1	Urban area of Bologna, Italy, in the synthetic 4-band SPOT-like image generated from the 7-band Landsat	[0.30, 1.50]	[0.70, 1.50]
	2	Coastal area of Sicily in the synthetic 4-band SPOT-like image generated from the 7-band Landsat	[0.40, 1.40]	[0.70, 1.50]
	3	Mountainous area in Northern Italy in the synthetic 4-band SPOT-like image generated from the 7-band Landsat	[0.40, 1.50]	[1.10, 1.50]
4-band Fuzzy AVSRC	1	Urban area of Bologna, Italy, in the synthetic 4-band AVHRR-like image generated from the 7-band Landsat	[0.20, 0.90]	[0.60, 1.50]
	2	Coastal area of Sicily in the synthetic 4-band AVHRR-like image generated from the 7-band Landsat	[0.20, 1.50]	[0.50, 1.50]
	3	Mountainous area in Northern Italy in the synthetic 4-band AVHRR-like image generated from the 7-band Landsat	[0.20, 0.60]	[1.00, 1.50]
4-band Fuzzy ISRC	1	Urban area of Bologna, Italy, in the synthetic 4-band IKONOS-like image generated from the 7-band Landsat	[0.00, 1.50]	[0.00, 1.50]
	2	Coastal area of Sicily in the synthetic 4-band IKONOS-like image generated from the 7-band Landsat	[0.00, 1.50]	[0.00, 1.50]
	3	Mountainous area in Northern Italy in the synthetic 4-band IKONOS-like image generated from the 7-band Landsat	[0.00, 1.50]	[0.80, 1.50]
Overlap across images and sensors of range values of P			[0.4, 0.5]	[1.10, 1.40]

multiple winners and $P \in [0.40, 0.50]$ to minimize mixed pixels (see Table VII). Within these ranges of choice, reasonable values of P are those at which the highest frequency of y -axis minima occurs in the graphs collected in Sections VI-A–D for the fuzzy LSRC (see Fig. 6), SSRC, AVSRC, and ISRC subsystems. These values are $P = 1.40$ to minimize multiple winners and $P = 0.50$ to minimize mixed pixels, respectively. According to Section V-C2, the former optimization value, $P = 1.40$, overcomes the latter.

To summarize, the final conclusion of this experimental work is that, based on evidence from data, the fuzzy SRC systems of systems adopts a predefined full bandwidth ΔB parameter of the fuzzy S- and Z-MFs equal to $\Delta B = 1.40 \times Th$, where parameter Th is found in [14, Tab. III]. Since, by definition of full bandwidth (refer to Section VI-A1), $0 < \Delta B = (2 \times \Delta b) = (c - b + b - a) = (c - a)$, with $a = [(1 - 0.5 \times P) \times Th] < b = Th < c = [(1 + 0.5 \times P) \times Th]$ in (1) and (2), then parameters a and b of the fuzzy S- and Z-MFs become $a = (0.3 \times Th)$ and $c = (1.7 \times Th)$.

This final choice is a compromise between the following: 1) the time required to develop and tune a physical-model-based system, such as the fuzzy SRC, which is typically very long [12], [23]; 2) the optimization across images and sensors of the fuzzy SRC system QIs (proposed in Section V-C2); and 3) the satisfaction of operational requirements proposed in Section I. In particular, this final choice implies that, like its crisp SRC counterpart, the novel fuzzy SRC is fully automatic [35], i.e., it requires neither user-defined parameters nor reference samples to run.

VII. SUMMARY AND CONCLUSIONS

In his well-known work on supervised fuzzy classification, Fanguiu Wang states that “if knowledge representation is poor, even sophisticated algorithms can produce inferior outputs” [25].

Motivated by Wang’s words about the importance of knowledge representation in an information processing device, this paper aims to enhance an innovative operational fully automated near-real-time SRC system of systems eligible for use as the pixel-based preliminary classification first stage of a two-stage stratified hierarchical hybrid RS-IUS architecture. As input, SRC requires an MS image radiometrically calibrated into TOARF or surface reflectance ρ values, the latter being an ideal (atmospheric noise-free) case of the former, i.e., $TOARF \supseteq \rho$. This radiometrically calibrated MS image can be acquired by all existing and future planned spaceborne optical imaging sensors provided with calibration metadata files in agreement with the QA4EO guidelines.

For the sake of simplicity, i.e., to reduce the number of system free parameters to be learnt by a human expert based on intuition, domain expertise, and evidence from data observation, the original presentation of SRC adopts crisp (hard) MFs unsuitable for dealing with component cover classes of mixed pixels (class mixture). To overcome this limitation, a novel fuzzy SRC system of systems is selected, designed, implemented, and compared against the crisp SRC, employed as a reference, in the preliminary classification of three test images acquired across time, space, and four sensors (one real and three synthesized).

Twelve experiments show that the proposed fuzzy SRC implementation, in which the full bandwidth parameter ΔB is computed as $\Delta B(Th) = 1.4 \times Th$, with the crisp threshold Th fixed according to [14, Tab. III], features the following.

- 1) It maintains the same degree of automation as the crisp SRC which is “fully automatic” (refer to Section I). Since both the crisp and fuzzy SRCs require neither user-defined parameters nor reference samples to run, their degree of automation cannot be surpassed by alternative approaches.
 - 2) On the average, it provides the best minimization of the number of multiple winners (refer to Section IV-F), i.e., it guarantees the best average separability between fuzzy MFs (refer to Section V-C2).
 - 3) Its output classification map is the same as that of its crisp counterpart excluding multiple winners, i.e., its robustness to changes in the input data set is the same as that of the crisp SRC.
 - 4) In addition to those generated by the crisp SRC, it provides as output three original products to model component cover classes of mixed pixels (refer to Section IV-E). This enhances the operational qualities of the fuzzy SRC with respect to the crisp SRC’s (refer to Section I).
 - 5) It replaces the hierarchical modular design of the crisp SRC decision tree with a flat (parallel horizontal) modular structure. The latter is easier to maintain and scale to changing users’ needs and sensor properties. This enhances the operational qualities of the fuzzy SRC with respect to the crisp SRC’s (refer to Section I).
 - 6) Point 5) means that the fuzzy SRC is single process and multithread while the crisp SRC decision tree is single process and single thread. As a consequence, in line with theory, to map a seven-band Landsat scene (8065×7000 pixels in size) on a standard desktop computer provided with a Dual Core Pentium processor, a sequential implementation of the fuzzy SRC employs 30% more computation time than its crisp counterpart, which requires approximately 6 min to run. The fuzzy SRC computational overload would reduce to zero in parallel computing (single process and multithread). It is noteworthy that the time interval between two consecutive spaceborne image acquisitions is not less than approximately 15 min (for the Meteosat Second Generation). This means that both the crisp and the fuzzy SRC can be considered near real time.
- The conclusion is that, in line with theory, operational qualities of the fuzzy and crisp SRCs are different, but both SRCs are suitable for the development of operational automatic near-real-time satellite-based measurement systems. This would open up new interdisciplinary research and market opportunities such as those listed below [15].
- 1) Integration into a complete desktop RS image processing software of the two-stage stratified hierarchical RS-IUS software toolbox employing SRC as its pixel-based preliminary classification first stage. This complete desktop RS image processing software would consist of an automatic, unifying (at the first stage), and standardized (e.g., based on RS data calibrated into physical radio-
 - metric units of measure), but incremental (at the second stage) software platform. It would make spaceborne optical image applications simple, reliable, and provided with traditional metrological/statistically based QIs as well as novel semantic-based QIs to achieve seamless intercomparison with alternative pertinent results. Based on experimental results collected in operational contexts [13]–[19], this complete desktop RS image processing software is expected to outperform existing scientific and commercial RS-IUSs such as those listed in Table I.
 - 2) Seamless integration of RS imagery with Geographic Information Systems (GIS). In RS common practice, SRC provides an automatic tool for the transformation of subsymbolic raster RS imagery into symbolic vector geospatial information managed by GIS.
 - 3) Integration of Internet-based satellite mapping on demand with virtual Earth geobrowsers such as the hugely popular Google Earth, NASA’s World Wind, and Microsoft Virtual Earth (see Fig. 11).
 - 4) Development of operational satellite-based measurement systems such as those envisaged under the ongoing international research programs GEOSS and GMES.
 - 5) Development of semantic querying systems of large-scale multisource RS image databases where SRC can be exploited as an automatic source of reference classification maps. This would represent a dramatic improvement over nonsemantic query modes currently available in image database retrieval systems based on text-driven query strategies and query by either an image, object, or multi-object example [64].
 - 6) Development of so-called fourth-generation future intelligent EO satellites [65] where the operational automatic near-real-time RS-IUS software proposed herein can be mounted onboard. The same consideration holds for ground receiving station which could be provided with an operational automatic “intelligent” data processing chain.
 - 7) Dissemination of advanced EO expertise, science, and technology capacity in developing countries and emerging countries. Automatic EO image understanding technologies are “democratic” in nature, i.e., eligible for use by all. In other words, EO researchers and institutions should perceive SRC as a novel technical opportunity to pursue ethical issues.

ACKNOWLEDGMENT

The author would like to thank the Editor-in-Chief, the Associate Editor, and the anonymous reviewers for their helpful comments and their patience in reviewing this paper, as well as their competence and willingness to help.

REFERENCES

- [1] G. Gutman, A. C. Janetos, C. O. Justice, E. F. Moran, J. F. Mustard, R. R. Rindfuss, D. Skole, B. L. Turner, II, M. A. Cochrane *et al.*, Eds., *Land Change Science*. Dordrecht, The Netherlands: Kluwer, 2004.
- [2] O. Sjahputera, C. H. Davis, B. Claywell, N. J. Hudson, J. M. Keller, M. G. Vincent, Y. Li, M. Klaric, and C. R. Shyu, “GeoCDX: An automated change detection and exploitation system for high resolution satellite imagery,” in *Proc. IGARSS*, Boston, MA, Jul. 6–11, 2008, pp. V-467–V-470, Paper FR4.101.1.

- [3] GEO, *The Global Earth Observation System of Systems (GEOSS) 10-Year Implementation Plan*, adopted Feb. 16, 2005. [Online]. Available: <http://www.earthobservations.org/docs/10-Year%20Implementation%20Plan.pdf>
- [4] [Online]. Available: <http://www.gmes.info>
- [5] P. Zamperoni, "Plus ça va, moins ça va," *Pattern Recognit. Lett.*, vol. 17, no. 7, pp. 671–677, Jun. 1996.
- [6] *eCognition User Guide 4*, Definiens Imaging GmbH, Munich, 2004.
- [7] R. Richter, *Atmospheric/Topographic Correction for Satellite Imagery—ATCOR-2/3 User Guide*, Wessling, Germany: DLR2006. [Online]. Available: http://www.geog.umontreal.ca/donnees/geo6333/atcor23_manual.pdf
- [8] T. Esch, M. Thiel, M. Bock, A. Roth, and S. Dech, "Improvement of image segmentation accuracy based on multiscale optimization procedure," *IEEE Geosci. Remote Sens. Lett.*, vol. 5, no. 3, pp. 463–467, Jul. 2008.
- [9] G. J. Hay and G. Castilla, "Object-based image analysis: Strengths, weaknesses, opportunities and threats (SWOT)," in *Proc. 1st Int. Conf. OBIA*, 2006. [Online]. Available: http://www.isprs.org/proceedings/XXXVII/4-C42/Papers/01_Opening%20Session/OBIA2006_Hay_Castilla.pdf
- [10] T. F. Cootes and C. J. Taylor, *Statistical Models of Appearance for Computer Vision, Imaging Science and Biomedical Engineering*. Manchester, U.K.: Univ. Manchester, Mar. 8, 2004.
- [11] T. Matsuyama and V. S.-S. Hwang, *SIGMA—A Knowledge-Based Aerial Image Understanding System*. New York: Plenum, 1990.
- [12] S. Liang, *Quantitative Remote Sensing of Land Surfaces*. Hoboken, NJ: Wiley, 2004.
- [13] A. Baraldi, "Impact of radiometric calibration and specifications of spaceborne optical imaging sensors on the development of operational automatic remote sensing image understanding systems," *IEEE J. Sel. Topics Appl. Earth Obs. Remote Sens.*, vol. 2, no. 2, pp. 104–134, Jun. 2009.
- [14] A. Baraldi, V. Puzzolo, P. Blonda, L. Bruzzone, and C. Tarantino, "Automatic spectral rule-based preliminary mapping of calibrated Landsat TM and ETM+images," *IEEE Trans. Geosci. Remote Sens.*, vol. 44, no. 9, pp. 2563–2586, Sep. 2006.
- [15] A. Baraldi, L. Durieux, D. Simonetti, G. Conchedda, F. Holecz, and P. Blonda, "Automatic spectral rule-based preliminary classification of radiometrically calibrated SPOT-4/-5/IRS, AVHRR/MSG, AATSR, IKONOS/QuickBird/OrbView/GeoEye and DMC/SPOT-1/-2 imagery—Part I: System design and implementation," *IEEE Trans. Geosci. Remote Sens.*, vol. 48, no. 3, pp. 1299–1325, Mar. 2010.
- [16] A. Baraldi, L. Durieux, D. Simonetti, G. Conchedda, F. Holecz, and P. Blonda, "Automatic spectral rule-based preliminary classification of radiometrically calibrated SPOT-4/-5/IRS, AVHRR/MSG, AATSR, IKONOS/QuickBird/OrbView/GeoEye and DMC/SPOT-1/-2 imagery—Part II: Classification accuracy assessment," *IEEE Trans. Geosci. Remote Sens.*, vol. 48, no. 3, pp. 1326–1354, Mar. 2010.
- [17] A. Baraldi, L. Durieux, D. Simonetti, G. Conchedda, F. Holecz, and P. Blonda, "Corrections to 'Automatic spectral rule-based preliminary classification of radiometrically calibrated SPOT-4/-5/IRS, AVHRR/MSG, AATSR, IKONOS/QuickBird/OrbView/GeoEye, and DMC/SPOT-1/-2 imagery,'" *IEEE Trans. Geosci. Remote Sens.*, vol. 48, no. 3, p. 1635, Mar. 2010.
- [18] A. Baraldi, M. Girona, and D. Simonetti, "Operational two-stage stratified topographic correction of spaceborne multi-spectral imagery employing an automatic spectral rule-based decision-tree preliminary classifier," *IEEE Trans. Geosci. Remote Sens.*, vol. 48, no. 1, pp. 112–146, Jan. 2010.
- [19] A. Baraldi, T. Wassenaar, and S. Kay, "Operational performance of an automatic preliminary spectral rule-based decision-tree classifier of spaceborne very high resolution optical images," *IEEE Trans. Geosci. Remote Sens.*, vol. 48, no. 9, pp. 3482–3502, Sep. 2010.
- [20] D. Marr, *Vision*. New York: Freeman, 1982.
- [21] A. K. Shackelford and C. H. Davis, "A hierarchical fuzzy classification approach for high-resolution multispectral data over urban areas," *IEEE Trans. Geosci. Remote Sens.*, vol. 41, no. 9, pp. 1920–1932, Sep. 2003.
- [22] K. Shackelford and C. H. Davis, "A combined fuzzy pixel-based and object-based approach for classification of high-resolution multispectral data over urban areas," *IEEE Trans. Geosci. Remote Sens.*, vol. 41, no. 10, pp. 2354–2363, Oct. 2003.
- [23] V. Cherkassky and F. Mulier, *Learning From Data: Concepts, Theory, and Methods*. New York: Wiley, 1998.
- [24] L. A. Zadeh, "Fuzzy sets," *Inf. Control*, vol. 8, pp. 338–353, 1965.
- [25] F. Wang, "Fuzzy supervised classification of remote sensing images," *IEEE Trans. Geosci. Remote Sens.*, vol. 28, no. 2, pp. 194–201, Mar. 1990.
- [26] M. Page-Jones, *The Practical Guide to Structured Systems Design*. Englewood Cliffs, NJ: Prentice-Hall, 1988.
- [27] W. Kaydos, *Operational Performance Measurement: Increasing Total Productivity*. Boca Raton, FL: CRC Press, 1999.
- [28] O. J. Tobias and R. Seara, "Image segmentation by histogram thresholding using fuzzy sets," *IEEE Trans. Image Process.*, vol. 11, no. 12, pp. 1457–1465, Dec. 2002.
- [29] R. G. Congalton and K. Green, *Assessing the Accuracy of Remotely Sensed Data*. Boca Raton, FL: Lewis Publishers, 1999.
- [30] G. M. Foody, "Status of land cover classification accuracy assessment," *Remote Sens. Environ.*, vol. 80, no. 1, pp. 185–201, Apr. 2002.
- [31] L. Wald, T. Ranchin, and M. Mangolini, "Fusion of satellite images of different spatial resolutions: Assessing the quality of resulting images," *Photogramm. Eng. Remote Sens.*, vol. 63, no. 6, pp. 691–697, Jun. 1997.
- [32] Z. Wang and A. C. Bovik, "A universal image quality index," *IEEE Signal Process. Lett.*, vol. 9, no. 3, pp. 81–84, Mar. 2002.
- [33] L. Alparone, S. Baronti, A. Garzelli, and F. Nencini, "A global quality measurement of pan-sharpened multispectral imagery," *IEEE Geosci. Remote Sens. Lett.*, vol. 1, no. 4, pp. 313–317, Oct. 2004.
- [34] L. Alparone, B. Aiazzi, S. Baronti, A. Garzelli, and F. Nencini, "A new method for MS+Pan image fusion assessment without reference," in *Proc. IEEE IGARSS*, Denver, CO, Jul. 31–Aug. 4, 2006, pp. 3802–3805.
- [35] Q. Yu and D. A. Clausi, "SAR sea-ice image analysis based on iterative region growing using semantics," *IEEE Trans. Geosci. Remote Sens.*, vol. 45, no. 12, pp. 3919–3931, Dec. 2007.
- [36] Y. V. Venkatesh and S. Kumar Raja, "On the classification of multispectral satellite images using the multilayer perceptron," *Pattern Recognit.*, vol. 36, no. 9, pp. 2161–2175, Sep. 2003.
- [37] A. K. Jain, R. Duin, and J. Mao, "Statistical pattern recognition: A review," *IEEE Trans. Pattern Anal. Mach. Intell.*, vol. 22, no. 1, pp. 4–37, Jan. 2000.
- [38] GEO/CEOSS, *A Quality Assurance Framework for Earth Observation*, Sep. 2008. [Online]. Available: http://qa4eo.org/docs/QA4EO_Principles_v4.0.pdf
- [39] E. Lunetta and C. Elvidge, *Remote Sensing Change Detection: Environmental Monitoring Methods and Applications*. London, U.K.: Taylor & Francis, 1999.
- [40] P. H. Swain and S. M. Davis, *Remote Sensing: The Quantitative Approach*. New York: McGraw-Hill, 1978.
- [41] S. Gopal and C. Woodcock, "Theory and methods for accuracy assessment of thematic maps using fuzzy sets," *Photogramm. Eng. Remote Sens.*, vol. 60, no. 2, pp. 181–188, Feb. 1994.
- [42] G. M. Foody, "Approaches for the production and evaluation of fuzzy land cover classifications from remotely-sensed data," *Int. J. Remote Sens.*, vol. 17, no. 7, pp. 1317–1340, May 1996.
- [43] G. J. Klir and T. A. Folger, *Fuzzy Sets, Uncertainty, and Information*. Englewood Cliffs, NJ: Prentice-Hall, 1988.
- [44] E. Binaghi, P. Brivio, P. Ghezzi, and A. Rampini, "A fuzzy set-based accuracy assessment of soft classification," *Pattern Recognit. Lett.*, vol. 20, no. 9, pp. 935–948, Sep. 1999.
- [45] G. Jäger and U. Benz, "Measures of classification accuracy based on fuzzy similarity," *IEEE Trans. Geosci. Remote Sens.*, vol. 38, no. 3, pp. 1462–1467, May 2000.
- [46] D. M. McKeown, W. A. Harvey, and J. McDermott, "Rule-based interpretation of aerial imagery," *IEEE Trans. Pattern Anal. Mach. Intell.*, vol. PAMI-7, no. 5, pp. 570–585, Sep. 1985.
- [47] J. Ton, J. Sticklen, and A. K. Jain, "Knowledge-based segmentation of Landsat images," *IEEE Trans. Geosci. Remote Sens.*, vol. 29, no. 2, pp. 222–231, Mar. 1991.
- [48] A. Laha, N. R. Pal, and J. Das, "Land cover classification using fuzzy rules and aggregation of contextual information through evidence theory," *IEEE Trans. Geosci. Remote Sens.*, vol. 44, no. 6, pp. 1633–1641, 2006.
- [49] MODIS Science Team, A. Strahler, D. Muchoney, J. Borak, M. Friedl, S. Gopal, E. Lambin, and A. Moody, *Modis Land Cover Product Algorithm Theoretical Basis Document (ATBD)*. [Online]. Available: http://modis.gsfc.nasa.gov/data/atbd/atbd_mod12.pdf
- [50] J. Chanussot, J. A. Benediktsson, and M. Fauvel, "Classification of remote sensing images from urban areas using a fuzzy possibilistic model," *IEEE Geosci. Remote Sens. Lett.*, vol. 3, no. 1, pp. 40–44, Jan. 2006.
- [51] M. Pesaresi and J. A. Benediktsson, "A new approach for the morphological segmentation of high-resolution satellite imagery," *IEEE Trans. Geosci. Remote Sens.*, vol. 39, no. 2, pp. 309–320, Feb. 2001.
- [52] C. Hudelot, J. Atif, and I. Bloch, "Fuzzy spatial relation ontology for image interpretation," *Fuzzy Sets Syst.*, vol. 159, no. 15, pp. 1929–1951, Aug. 2008.
- [53] G. Sagerer and H. Niemann, "Semantic networks for understanding scenes," in *Advances in Computer Vision and Machine Intelligence*. New York: Plenum, 1997.
- [54] InterIMAGE Operation Guide, (beta version 0.09). [Online]. Available: <http://www.lvc.ele.puc-rio.br/projects/interimage/documentation/>
- [55] C. Mason and E. R. Kandel, "Central visual pathways," in *Principles of Neural Science*, E. Kandel and J. Schwartz, Eds. Norwalk, CT: Appleton and Lange, 1991, pp. 420–439.

- [56] P. Gouras, "Color vision," in *Principles of Neural Science*, E. Kandel and J. Schwartz, Eds. Norwalk, CT: Appleton and Lange, 1991, pp. 467–479.
- [57] E. R. Kandel, "Perception of motion, depth and form," in *Principles of Neural Science*, E. Kandel and J. Schwartz, Eds. Norwalk, CT: Appleton and Lange, 1991, pp. 441–466.
- [58] H. R. Wilson and J. R. Bergen, "A four mechanism model for threshold spatial vision," *Vis. Res.*, vol. 19, no. 1, pp. 19–32, 1979.
- [59] T. Lillesand and R. Kiefer, *Remote Sensing and Image Interpretation*. New York: Wiley, 1994.
- [60] A. Di Gregorio and L. Jansen, "Land Cover Classification System (LCCS): Classification Concepts and User Manual," *FAO Corporate Document Repository*. [Online]. Available: <http://www.fao.org/DOCREP/003/X0596E/X0596e00.htm>
- [61] P. Mather, *Computer Processing of Remotely-Sensed Images—An Introduction*. Chichester, U.K.: Wiley, 1994.
- [62] L. Prechelt, "A quantitative study of experimental evaluations of neural network learning algorithms: Current research practice," *Neural Netw.*, vol. 9, no. 3, pp. 457–462, Apr. 1996.
- [63] L. Delves, R. Wilkinson, C. Oliver, and R. White, "Comparing the performance of SAR image segmentation algorithms," *Int. J. Remote Sens.*, vol. 13, no. 11, pp. 2121–2149, 1992.
- [64] C.-R. Shyu, M. Klaric, G. J. Scott, A. S. Barb, C. H. Davis, and K. Palaniappan, "GeoIRIS: Geospatial information retrieval and indexing system—Content mining, semantics modeling, and complex queries," *IEEE Trans. Geosci. Remote Sens.*, vol. 45, no. 4, pp. 839–852, Apr. 2007.
- [65] G. Zhou, O. Baysal, and M. Kafatos, Eds., *Future Intelligent Earth Observing Satellites*: Hierophantes Press, ISBN: 0-9727940-0-x, 2002, ch. 1, pp. 1–18.
- [66] I. Bloch, "Information combination operators for data fusion: A comparative review with classification," *IEEE Trans. Syst., Man, Cybern. A, Syst., Humans*, vol. 26, no. 1, pp. 52–67, Jan. 1996.



Andrea Baraldi was born in Modena, Italy, in 1963. He received the Laurea (M.S.) degree in electronic engineering from the University of Bologna, Bologna, Italy, in 1989. His master's thesis focused on the development of segmentation and classification algorithms for remotely sensed optical imagery.

From 1989 to 1990, he was a Research Associate with the Centro di Studio per l'Interazione Operatore-Calcolatore, National Research Council (CNR), Bologna, and served in the army with the Istituto Geografico Militare, Florence, Italy, working on satellite image classifiers and geographic information systems (GISs). As a Consultant with the European Space Research Institute, European Space Agency, Frascati, Italy, he worked on object-oriented applications for GIS from 1991 to 1993. From December 1997 to June 1999, he was assigned with a postdoctoral fellowship in Artificial Intelligence at the International Computer Science Institute, Berkeley, CA. From 2000 to 2002, as a Postdoc Researcher, he joined the Global Vegetation Monitoring unit of the Institute for Environment and Sustainability (IES), European Commission Joint Research Centre (JRC), Ispra, Italy, in the development and validation of algorithms for forest classification of radar mosaics at continental scale. From 2005 to 2009, at the IES—Spatial Data Infrastructure, JRC, he was involved with satellite optical image calibration, classification, and mosaicking at continental scale. Since his master's thesis, he has continued his collaboration with the Istituto di Scienze dell'Atmosfera e del Clima, CNR, Bologna, and the Istituto di Studi di Sistemi Intelligenti per l'Automazione, CNR, Bari, Italy. He is currently a Research Associate Professor with the Department of Geography, University of Maryland, College Park, MD. His main interests center on image understanding, with special emphasis on the development of operational automatic hierarchical multisource multiresolution spaceborne image understanding systems consistent with biological vision. From 2001 to 2006, he served as an Associate Editor of the IEEE TRANSACTIONS ON NEURAL NETWORKS.